
RESEARCH ARTICLE

Hydro-micromechanical modeling of wave propagation in saturated granular media

Hongyang Cheng¹ | Stefan Luding¹ | Nicolás Rivas² |
Jens Harting^{2,3} | Vanessa Magnanimo¹

¹Multi-Scale Mechanics (MSM), Faculty of Engineering Technology, MESA+, University of Twente, P.O. Box 217, 7500 AE Enschede, The Netherlands

²Forschungszentrum Jülich, Helmholtz Institute Erlangen-Nürnberg for Renewable Energy (IEK-11), Fürther Straße 248, 90429 Nürnberg, Germany

³Department of Applied Physics, Eindhoven University of Technology, P.O. Box 513, 5600 MB Eindhoven, The Netherlands

Correspondence

Hongyang Cheng, Multi-Scale Mechanics (MSM), Faculty of Engineering Technology, MESA+, University of Twente, P.O. Box 217, 7500 AE Enschede, The Netherlands
Email: h.cheng@utwente.nl

Funding information

We acknowledge support from the European Space Agency (ESA) contract 4000115113 'Soft Matter Dynamics' and the European Cooperation in Science and Technology (COST) Action MP1305 'Flowing matter'

Biot's theory predicts the wave velocities of a saturated poroelastic granular medium from the elastic properties, density and geometry of its dry solid matrix and the pore fluid, neglecting the interaction between constituent particles and local flow. However, when the frequencies become high and the wavelengths comparable with particle size, the details of the microstructure start to play an important role. Here, a novel hydro-micromechanical numerical model is proposed by coupling the lattice Boltzmann method (LBM) with the discrete element method (DEM). The model allows to investigate the details of the particle-fluid interaction during propagation of elastic waves. While the DEM is tracking the translational and rotational motion of each solid particle, the LBM can resolve the pore-scale hydrodynamics. Solid and fluid phases are two-way coupled through momentum exchange. The coupling scheme is benchmarked with the terminal velocity of a single sphere settling in a fluid. To mimic a pressure wave entering a saturated granular medium, an oscillating pressure boundary condition on the fluid is implemented and benchmarked with one-dimensional wave equations. Using a face centered cubic structure, the effects of input waveforms and frequencies on the dispersion relations are investigated. Finally, the wave velocities at various effective confining pressures predicted by the numerical

model are compared with with Biot's analytical solution, and a very good agreement is found. In addition to the pressure and shear waves, slow compressional waves are observed in the simulations, as predicted by Biot's theory.

KEYWORDS

Wave propagation, Lattice Boltzmann method, Discrete element method, Fluid-solid coupling, Acoustic source, Biot's theory

1 | INTRODUCTION

Understanding wave propagation in saturated and dry granular media is vital for non-destructive soil testing [1, 2, 3], seismicity analysis [4, 5, 6] and oil exploration [7, 8], among others. Extensive work has been done to understand the dispersion and attenuation properties of dry granular media in both laboratory tests and computer simulations [9, 10, 11, 12]. The kinematics at the microscale associated with macroscopic wave propagation in dry granular media can be reproduced with the discrete element method (DEM) [13, 14, 15, 11], given that parameters are properly calibrated [16, 17, 18]. For wave propagation in fully/partially saturated granular media [19], it becomes necessary to take into account the momentum and energy exchange between fluid, solid and/or gas phases in a fully coupled manner.

Depending on the spatial and temporal resolution of the hydrodynamic interactions in the pore fluid, various coupled methods have been proposed for dense or loose granular materials submerged in viscous fluids [20, 21, 22]. While the conventional computational fluid dynamics (CFD) methods couple the drag forces on solid particles locally into the Navier-Stokes equations [23], direct numerical simulation techniques like the lattice Boltzmann method (LBM) [24, 25] aim to mesoscopically resolve the hydrodynamic interactions and the momentum balance [26, 27, 28, 29] on the no-slip fluid-solid interfaces. Conventional CFD methods are sufficient for modeling dilute suspensions of particles in which local pore-scale fluid flow is not important, whereas direct numerical simulations are better suited for fully/partially saturated dense granular/porous media. Unlike standard continuum approaches which require significant computational costs for adaptive remeshing around the particles, the LBM avoids remeshing by projecting particle shapes on an Eulerian lattice to advect and bounce back the fluid. The advantage of the LBM lies in the locality of the collisional and streaming operations of fluid "particles" and the explicit time-stepping scheme, which make LBM simulations highly parallelizable. For geotechnical and geophysical applications in which the saturated granular materials are typically dense, accurately predicting pressure gradients in the pore space is pivotal in reproducing fluid-solid interaction processes such as consolidation [30] and wave propagation [31]. Therefore, in this work the LBM and the DEM are coupled to respectively resolve the pore-scale fluid flow and the motions and interparticle forces of solid particles.

The key aspect of fluid-solid coupling for LB-DEM is the calculations of hydrodynamic forces on solid particles and the influence of particle motions on the flow field. Ladd and Aidun [32, 25] proposed the momentum exchange method which applies the no-slip boundary condition along the links between fluid and solid nodes. The other family of fluid-solid coupling is the Noble-Torczynski method [33]. Instead of bouncing back the fluid along the links, the Noble-Torczynski method modifies local collisional operator with the solid volume fractions of the fluid cells occupied by the solid particles. Extensive comparative studies have been carried out to investigate the accuracy and suitability of the two coupling schemes and their variants [34, 35]. The Noble-Torczynski method appears to cause numerical dissipation, and the accuracy depends on the relaxation parameter that is related to fluid viscosity. LB-DEM simulations using the

momentum exchange method (MEM) is prone to high-frequency fluctuation because of the binary transition between the fluid and solid nodes. Nevertheless, the noises appear at a spatial scale much smaller than particle sizes and thus will be smeared out after performing local volume averaging [36, 37, 38, 39]. It is expected that as long as the resolution of the solid particles is sufficiently high, the high-frequency noises will not affect the pore-scale flow behavior. Therefore, in this work the MEM is employed for fluid-solid coupling.

Recent applications of the LBM in acoustics has demonstrated the capability of the LBM to capture weak pressure fluctuations with high accuracy. The acoustic behavior reproduced using the point sources in [40] were benchmarked with wave equations in different coordinate systems. The monopole acoustic source was later extended to multipole in both 2D [41] and 3D [42]. In this work, however, only pressure waves in the saturated granular systems are simulated. The propagation of pressure waves in a saturated granular media is consistent with the original setup envisaged by Biot [31]. The primary goal in the present work is to implement an oscillating pressure boundary condition to mimic acoustic waves coming from the fluid and to test its performance in LB-DEM simulations of wave propagation in saturated granular media.

Biot's theory predicts that the compressional(P)-wave typically travels faster in a saturated granular medium than in its dry solid matrix, and the shear(S)-wave velocity is reduced because of the inertia coupling caused by the relative acceleration between the solid and the pore fluid. The theory provides a set of balance equations that describe the macroscopic velocities of the pore fluid and solid matrix in the saturated poroelastic granular material. Given the continuum nature of the theory, both the pore- and micro-structures are assumed to be homogeneous, neglecting their contribution to the pore-scale fluid flow and the effective elastic moduli. However, the effect of microstructures should come into play when the wavelengths are a few times bigger than the sizes of the constituent solid particles. To revisit the wave propagation mechanisms as described in Biot's theory, direct numerical simulations of the multiphase processes involved are needed. Therefore, a hydro-micromechanical model is developed, with the novelty consists in the fluid-coupling scheme and the oscillating pressure boundary within the framework of the coupled LB-DEM. The hydro-micromechanical model allows for investigations of the dispersion relations and attenuation of saturated poroelastic granular media at various effective confining pressures and wave frequencies, so that the numerical predictions can be compared with Biot's analytical solution. Other governing mechanisms including the highly attenuated, diffusive slow wave are explored as well.

The remainder of this paper is organized as follows. Sec. 2 explains the fundamentals of the hydro-micromechanical model, including the LBM for simulating fluid in Sec. 2.1, the DEM for solid particles in Sec. 2.2, the fluid-solid interactions in Sec. 2.3 and the acoustic source in Sec. 2.4. Sec. 3 benchmarks the fluid-solid coupling scheme and the acoustic source with their respective analytical solutions. The hydro-micromechanical model is applied to simulate elastic wave propagation in fully saturated face-cubic-centered microstructures in Sec. 4, with the model parameters and unit conversion highlighted in Sec. 4.2. The influence of pore fluid on the dispersion relations is discussed in Sec. 4.3 and the effect of acoustic source investigated in Sec. 4.4. Sec. 5 shows the comparison of the numerical predictions and the analytical values predicted by Biot's equations and the numerical evidence of the slow compressional wave. Conclusions are drawn in Sec. 6.

2 | HYDRO-MICROMECHANICAL MODEL

The local hydrodynamics in the pore space of a granular medium is modeled by solving the discrete Boltzmann equation with a Bhatnagar-Gross-Krook (BGK) collision operator. The BGK operator uses a single relaxation time for the probability distribution of local fluid velocities towards an equilibrium distribution. Interactions between contacting

solid particles and their microstructural evolution are modeled with the discrete element method (DEM). The fluid-solid coupling scheme is implemented following the momentum exchange method [43, 44, 25], which takes into account the hydrodynamic forces on the solid skeleton and the influence of particle motions on the fluid flow. An oscillating pressure boundary condition is employed to send acoustic waves from the fluid into the saturated granular media.

2.1 | Hydrodynamics

The Boltzmann equation describes the evolution of a collection of particles via their associated probability density functions in the space and velocity phase-space. Interactions between particles are accounted by a collision operator, which we take here to have the simple Bhatnagar-Gross-Krook (BGK) form, such that,

$$\left(\frac{\partial}{\partial t} + \boldsymbol{\xi} \cdot \nabla_{\mathbf{x}} + \boldsymbol{\Phi}_B \cdot \nabla_{\boldsymbol{\xi}} \right) f = \frac{1}{\tau} (\bar{f} - f) \quad (1)$$

Here, $f(\mathbf{x}, \boldsymbol{\xi}, t)$ is the probability distribution function associated with particles at position \mathbf{x} with velocity $\boldsymbol{\xi}$; $\boldsymbol{\Phi}_B$ is an external force and τ the relaxation time during which local distributions are relaxed to the equilibrium distribution $\bar{f}(\mathbf{x}, \boldsymbol{\xi}, t)$. The macroscopic fluid density and velocity are retrieved via $\rho = \int f \Delta \boldsymbol{\xi}$ and $\mathbf{u} = (1/\rho) \int \boldsymbol{\xi} f \Delta \boldsymbol{\xi}$. If at equilibrium the Maxwell-Boltzmann distribution is considered,

$$\bar{f}(\mathbf{x}, \mathbf{v}, t) = \rho \left(\frac{\rho}{2\pi p} \right)^{3/2} \exp \left(- \frac{\rho \mathbf{v}^2}{2p} \right), \quad (2)$$

with $\mathbf{v} = \boldsymbol{\xi} - \mathbf{u}$ and p the pressure, it can be shown that through the Chapman-Enskog expansion, with the Knudsen number sufficiently small, the Navier-Stokes equations are recovered.

The LBM solves the Boltzmann equation discretized in space and velocity. Having its origin in statistical mechanics, the variables in LBM are probability distribution functions on a Cartesian lattice rather than macroscopic pressure and velocity in conventional CFD methods. At each time step, fluid particles on each lattice node are streamed to their immediate neighboring nodes along certain directions. The collision operator is then directly computed at each lattice cite from the macroscopic variables.

The discretization of velocity space requires a finite set of velocity vectors along which the fluid particles can propagate and collide, reducing the continuous distribution function $f(\mathbf{x}, \boldsymbol{\xi}, t)$ to $f_d(\mathbf{x}, t)$ on the discrete velocity directions. In this work, we use the D3Q19 lattice (3 dimensions, 19 velocity vectors) with spacing Δx , such that fluid particles can propagate to the nearest and next-nearest neighbors at each time step Δt . The discrete velocity vectors $\mathbf{c}_d (d = 1 \dots 19)$ are defined as

$$\mathbf{c}_d = c \begin{bmatrix} 1 & -1 & 0 & 0 & 0 & 0 & 1 & 1 & 1 & 1 & -1 & -1 & -1 & -1 & 0 & 0 & 0 & 0 & 0 \\ 0 & 0 & 1 & -1 & 0 & 0 & 1 & -1 & 0 & 0 & 1 & -1 & 0 & 0 & 1 & 1 & -1 & -1 & 0 \\ 0 & 0 & 0 & 0 & 1 & -1 & 0 & 0 & 1 & -1 & 0 & 0 & 1 & -1 & 1 & -1 & 1 & -1 & 0 \end{bmatrix}, \quad (3)$$

with $c = \Delta x / \Delta t$, and illustrated in Fig. 1. By adopting the discretizations above, the BGK collisional operator Eq. 1 can be rewritten as

$$\bar{f}_d(\mathbf{x}, t) = f_d(\mathbf{x}, t) + \frac{\Delta t}{\tau} \left(f_d^{eq}(\mathbf{x}, t) - f_d(\mathbf{x}, t) \right), \quad (4)$$

$$f_d(\mathbf{x} + \mathbf{c}_d \Delta t, t + \Delta t) = \bar{f}_d(\mathbf{x}, t), \quad (5)$$

FIGURE 1 The geometry of the D3Q19 lattice with the lattice vectors \mathbf{c}_d in Eq. 3. (figure from [53])

where $\bar{f}_d(\mathbf{x}, t)$ are the post-collision values to be distributed to the corresponding lattice neighbors in the succeeding streaming step. The dimensionless relaxation time $\tau \in (0.5, \infty)$ implicitly determines the kinematic viscosity ν , together with the lattice spacing Δx and the time step Δt via $\nu = (\tau - \Delta t/2)c_s^2$. The lattice speed of sound $c_s = \Delta x/\sqrt{3}\Delta t$ for the D3Q19 lattice is defined by the discretizations. After expansion to second order, the equilibrium distribution $f_d^{eq}(\mathbf{x}, t)$ in Eq. 2 becomes

$$f_d^{eq} = w_d \rho \left[1 + \frac{\mathbf{c}_d \cdot \mathbf{u}}{c_s^2} + \frac{(\mathbf{c}_d \cdot \mathbf{u})^2}{2c_s^4} - \frac{\mathbf{u} \cdot \mathbf{u}}{2c_s^2} \right], \quad (6)$$

where the macroscopic fluid density $\rho = \rho_f + \rho'$, with the mean density ρ_f and the off-equilibrium density ρ' . Together with the macroscopic fluid velocity these are calculated via the zeroth and first moments of the distribution functions $f_d(\mathbf{x}, t)$ as,

$$\rho = \sum_d f_d, \quad \mathbf{u} = \frac{1}{\rho} \sum_d f_d \mathbf{c}_d. \quad (7)$$

The lattice weights w_d in Eq. 6 for a D3Q19 LB model are given as follows.

$$w_d = \begin{cases} 1/3, & \text{if } |\mathbf{c}_d| = 0, \\ 1/18, & \text{if } |\mathbf{c}_d| = \Delta x/\Delta t, \\ 1/36, & \text{if } |\mathbf{c}_d| = \sqrt{2}(\Delta x/\Delta t). \end{cases} \quad (8)$$

2.2 | Micromechanics

The DEM represents granular materials as packings of solid particles with simplified geometries (e.g., spheres) and vanishingly small interparticle overlaps. This way, the particles in contact can interact with their neighbors via repulsive

springs and viscous dashpots, resulting in relative motion between the particles. Generally, the time step in DEM is very small in order to sufficiently resolve collisions or oscillations in time. Once all the forces acting on each particle, either from interacting neighbors or from the surrounding fluid are known, the kinematics of each particle are updated by Newton's second law within the explicit time integration scheme. The equations of translational and rotational motion for each solid particle are

$$m\dot{\mathbf{V}}_p = \sum_{c \in N_p^c} \mathbf{F}_c + \mathbf{F}_{f-s} + \mathbf{F}_g, \quad (9)$$

$$\mathbf{I}\dot{\boldsymbol{\Omega}}_p = \sum_{c \in N_p^c} (\mathbf{X}_c - \mathbf{X}_p)\mathbf{F}_c + \mathbf{T}_{f-s}, \quad (10)$$

where m and \mathbf{I} are the mass and the moment of inertia of the particle, with \mathbf{V}_p and $\boldsymbol{\Omega}_p$ the resultant linear and angular velocities at the center \mathbf{X}_p . \mathbf{F}_c is a contact force applied on the particle, with c summing over the contact points N_p^c ; $\mathbf{X}_c - \mathbf{X}_p$ is the vector connecting the contact point at \mathbf{X}_c to the center position \mathbf{X}_p ; \mathbf{F}_{f-s} and \mathbf{T}_{f-s} are the hydrodynamic force and moment acting on the particle, and \mathbf{F}_g the external body force. The superposed dot represents a time derivative, e.g., $\dot{\mathbf{V}}_p = \dot{\mathbf{X}}_p$.

The interparticle force between two contacting solid particles can be described by contact-level force-displacement laws in normal and tangential directions, i.e., $\mathbf{F}_c = \mathbf{F}_n + \mathbf{F}_t$. The tangential component of the force is constrained by a Coulomb type yield criterion. For two contacting spheres with a normal overlap \mathbf{u}_n , a relative tangential displacement $\Delta\mathbf{u}_t$, the interparticle normal and tangential forces \mathbf{F}_n and $\Delta\mathbf{F}_t$ can be calculated as

$$\mathbf{F}_n = \frac{2E_p\mathbf{u}_n}{3(1-\nu_p^2)}\sqrt{R^*\|\mathbf{u}_n\|}, \quad (11)$$

$$\Delta\mathbf{F}_t = \frac{2E_p\Delta\mathbf{u}_t}{(1+\nu_p)(2-\nu_p)}\sqrt{R^*\|\mathbf{u}_n\|} \quad \text{and} \quad \|\mathbf{F}_t\| \leq \mu\|\mathbf{F}_n\|, \quad (12)$$

where E_p and ν_p are the contact-level Young's modulus and Poisson's ratio, μ is the interparticle friction coefficient, R^* is the equivalent radius defined as $1/(1/R_1 + 1/R_2)$, where R_1 and R_2 are the radii of the two particles. From the contact force network in a given microstructural configuration, the effective stress tensor is given by the average over the particle assembly

$$\boldsymbol{\sigma}' = \frac{1}{V} \sum_{c \in N_c} \mathbf{F}_c \otimes \mathbf{d}_c \quad (13)$$

where $\boldsymbol{\sigma}'$ is the bulk stress tensor, N_c is the total number of contacts contained within the force network, V is the total volume of the granular assembly including the pore space, and \mathbf{d}_c is the branch vector connecting the centers of each pair of contacting particles.

2.3 | Fluid-solid coupling scheme

Boundary conditions in the LBM are implemented by constructing the distribution functions from physical boundary constraints such as pressure and velocity. The momentum exchange method (MEM) was first presented by Ladd [43] and Aidun [44] for handling moving boundary conditions between fluid and solid. The main idea is to project solid obstacles such as solid particles onto the lattice, marking the nodes contained by the particles as solid and the rest as fluid. A solid node has at least one link with neighboring fluid nodes. Along the links, as shown in Fig. 2, momentum is exchanged

and no-slip boundary conditions, i.e., the macroscopic flow velocity matching the particle's velocity, are applied on the solid surface. From the exchanged momentum, the hydrodynamic force acting on the particle can be obtained as a consequence of the no-slip condition applied to fluid advecting towards solid nodes. Fig. 2 shows an illustration of the coupling scheme. In this work, fluid advecting onto the surface of a solid particle is simply bounced back half way

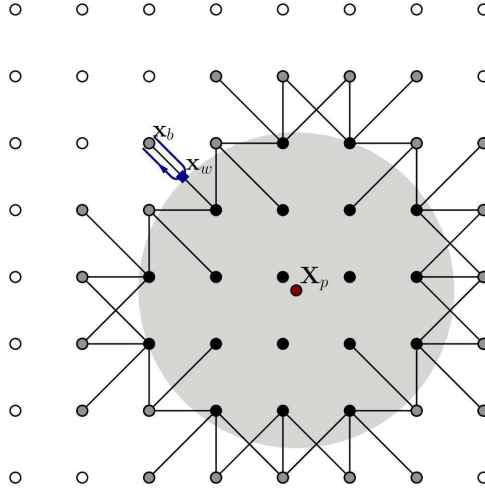


FIGURE 2 Staircase approximation of a circle. The discretization of a circle requires the identification and conversion between fluid nodes (white circles), boundary nodes (gray circles) and solid nodes (black circles). A boundary node (blue square) is located in midway between the fluid and solid nodes at x_w . Fluid particles advecting along the fluid-solid links $c_{d_{f-s}}$ are bounced back at x_w . (figure redrawn from [25]).

between the solid and the fluid nodes by setting

$$f_{d^*}(\mathbf{x}, t + \Delta t) = \tilde{f}_d(\mathbf{x}, t) - 2 \frac{w_d}{c_s^2} \rho \mathbf{V}_b(\mathbf{x}_b, t) \cdot \mathbf{c}_d, \quad (14)$$

where d^* denotes the direction opposite to d such that $\mathbf{c}_{d^*} = -\mathbf{c}_d^*$, and $\mathbf{V}_b(\mathbf{x}_b, t) = \mathbf{V}_p(t) + \boldsymbol{\Omega}_p(t) \times (\mathbf{x}_b - \mathbf{X}_p(t))$ is the velocity at the boundary position \mathbf{x}_b located midway between the fluid and the solid nodes. The second term of Eq. 14, in addition to the standard bounce-back solid boundary, is contributed by the motion of the particle moving across the lattice. Following the momentum exchange idea, the force $\mathbf{F}_{d_{f-s}}$ transferred to the solid particle at position \mathbf{x}_b over a fluid-solid link $f-s$ from every bounce-back collision is

$$\mathbf{F}_{d_{f-s}}(\mathbf{x}_b, t) = \frac{(\Delta x)^3}{\Delta t} (\mathbf{c}_{d_{f-s}} \tilde{f}_d(\mathbf{x}, t) - \mathbf{c}_{d_{f-s}^*} f_{d_{f-s}^*}(\mathbf{x}, t + \Delta t)). \quad (15)$$

It can be seen from Eq. 15 that the hydrodynamic forces coupled to the solid particle are a direct consequence of the unbalanced momenta along the fluid-solid links.

As the particle moves and occupies neighboring fluid nodes, the fluid nodes at $\mathbf{x}_{f \rightarrow s}$ are converted to solid ones. During the conversion, the momentum on the fluid nodes has to be transferred to the particle, so that the global

momentum is conserved. Therefore, a correction term is added to the fluid-solid coupling,

$$\mathbf{F}_{f \rightarrow s} = -\frac{\rho \mathbf{u} (\Delta x)^3}{\Delta t}. \quad (16)$$

The lattice nodes regarded as solid nodes do not participate in the LBM calculation cycles, namely Eqs. 4–6. However, as the particle moves away from its solid nodes, the uncovered solid nodes at $\mathbf{x}_{s \rightarrow f}$ have to be converted back to the fluid phase. In order to ensure a consistent reconstruction of the probability distribution on each new fluid node, the velocity of the solid particle therein is used to calculate the equilibrium distributions in Eq. 6, and the new density corresponds to the average of neighboring nodes. Similar to Eq. 16, the final correction that takes the additional momentum away from the particle is

$$\mathbf{F}_{s \rightarrow f} = \frac{\bar{\rho} \mathbf{u} (\Delta x)^3}{\Delta t}. \quad (17)$$

Therefore, the total force \mathbf{F}_{f-s} and torque \mathbf{T}_{f-s} acting on a solid particle is obtained from: (i) the forces given by the momentum exchange, with the sum running over the fluid-solid links and then the boundary nodes, and (ii) the forces resulting from the destruction and reconstruction of the relevant fluid nodes, namely

$$\mathbf{F}_{f-s}(t) = \sum_{\mathbf{x}_b} \sum_{d_{f-s}} \mathbf{F}_{d_{f-s}}(\mathbf{x}_b, t) + \sum_{\mathbf{x}_{f \rightarrow s}} \mathbf{F}_{f \rightarrow s} + \sum_{\mathbf{x}_{s \rightarrow f}} \mathbf{F}_{s \rightarrow f}, \quad (18)$$

$$\begin{aligned} \mathbf{T}_{f-s}(t) = & \sum_{\mathbf{x}_b} \sum_{d_{f-s}} (\mathbf{x}_b - \mathbf{X}_p) \times \mathbf{F}_{d_{f-s}}(\mathbf{x}_b, t) + \sum_{\mathbf{x}_{f \rightarrow s}} (\mathbf{x}_{f \rightarrow s} - \mathbf{X}_p) \times \mathbf{F}_{f \rightarrow s} \\ & + \sum_{\mathbf{x}_{s \rightarrow f}} (\mathbf{x}_{s \rightarrow f} - \mathbf{X}_p) \times \mathbf{F}_{s \rightarrow f}. \end{aligned} \quad (19)$$

2.4 | Acoustic source for LBM simulations

The acoustic source for simulating pressure waves entering a fluid consists in enforcing the boundary nodes to emit the correct numbers of fluid particles, which macroscopically leads to oscillations in the velocity component along the propagation direction. A pressure boundary condition is first needed. To model fluid flow in granular media, the pressure boundary conditions are typically set with constant local densities. The flow is then driven by an imposed pressure gradient between two opposite boundaries. This approach was first suggested by Zou and He for the D2Q9 lattice [45] and later extended to the D3Q15 and D3Q19 lattice by Kutay et al. [46] and Hecht and Harting [47]. At a pressure boundary, the unknown velocity component in the flow direction can be determined from the two known velocity components and a given density ρ . For a D3Q19 LB model, this is done by enforcing the bounce-back rule to the non-equilibrium part of the distribution $f_d - f_d^{eq}$ at the boundary, namely $f_d - f_d^{eq} = f_{d^*} - f_{d^*}^{eq}$. Therefore, for the pressure boundary located at the bottom ($x_z = 0$) of the D3Q19 lattice in Fig. 1, the unknown values of the distribution

function f_5, f_9, f_{13}, f_{15} and f_{17} can be calculated as

$$f_5 = f_3 + \frac{\rho u_z}{3c}, \quad (20)$$

$$f_9 = f_{14} + \frac{\rho(u_z + u_x)}{6c} - N_x^z, \quad (21)$$

$$f_{13} = f_{10} + \frac{\rho(u_z - u_x)}{6c} + N_x^z, \quad (22)$$

$$f_{15} = f_{18} + \frac{\rho(u_z + u_y)}{6c} - N_y^z, \quad (23)$$

$$f_{17} = f_{16} + \frac{\rho(u_z - u_y)}{6c} + N_y^z, \quad (24)$$

where $N_x^z = \frac{1}{2}(f_1 + f_7 + f_8 - f_2 - f_{11} - f_{12}) + \frac{\rho u_x}{3c}$ and $N_y^z = \frac{1}{2}(f_3 + f_7 + f_{11} - f_4 - f_8 - f_{12}) + \frac{\rho u_y}{3c}$ are the transverse momentum corrections along tangential directions that vanish at equilibrium, but become non-zero when boundary-induced stresses are present.

To send out plane waves from the pressure boundaries, the local densities at the boundary nodes are locked to periodic functions that oscillate around ρ_f for finite time steps. A similar acoustic source was proposed in [40] and verified against the analytic solutions of viscously damped sinusoidal waves. For the pressure boundary nodes which agitate sinusoidal plane waves, the local densities vary according to

$$\rho(t) = \rho_f + \rho' \sin(\omega t), \quad (t \leq t_n), \quad (25)$$

where ω is the input angular frequency and t_n the number of time steps during which $\rho(t) \neq \rho_f$. Because elastic wave propagation is a linear phenomenon and the Navier-Stokes equation can only be assumed to be linear for small disturbances, it is important to ensure $\rho' \ll \rho_f$ so that nonlinear wave effects are avoided. Moreover, the computational Mach number $M = |\mathbf{u}_{max}|/c$ has to be much smaller than 1.0, because the macroscopic quantities given by the discrete-velocity Boltzmann equation converge to the solution of the incompressible Navier-Stokes equation with order M^2 .

3 | VERIFICATION OF THE HYDRO-MICROMECHANICAL MODEL

The fluid-solid coupling scheme and the acoustic source are benchmarked with single particle sedimentation and one-dimensional wave propagation in a pure fluid. The terminal velocities of a single sphere and the acoustic propagation and attenuation in a fluid are obtained from the simulations, and then compared with the respective analytical solutions. To verify the acoustic source for saturated granular systems, a granular chain of spherical particles is inserted into the same fluid domain. Elastic waves are agitated by the same acoustic source as in the second benchmark. Three additional benchmarks, including the propagation of an elastic wave in the same system in dry condition, are used to ascertain that the acoustic response due to the presence of the particles and their motions is reproduced correctly, before introducing more complex microstructure. In all the simulations below, lattice units are used consistently for convenience, i.e., the lattice spacing $\Delta x = 1$ and the time step $\Delta t = 1$ (for both LB and DE parts), which results in the lattice speed of sound $c_s = 1/\sqrt{3}$. The particles are monodisperse spheres with the radius $R = R_0 + \|\mathbf{u}_n\|/2$, where $R_0 = 5$ and $\|\mathbf{u}_n\| = 0.01$.

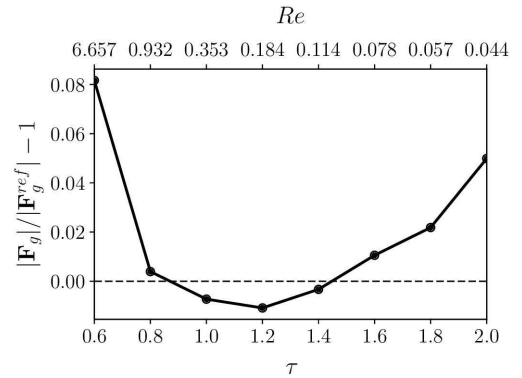
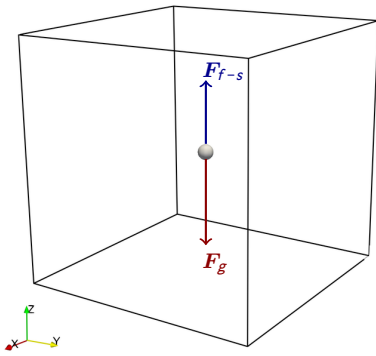
3.1 | Terminal velocity of a single sphere

Fig. 3a shows the simulation setup to obtain the terminal velocity of a single sphere settling in a viscous fluid. The sphere is released at the center of the cubic fluid domain ($160 \times 160 \times 160$). Periodic boundary conditions are adopted at all sides of the cubic domain. The sedimentation of the sphere is driven by a constant body force that accelerates and thus gives rise to a drag force on the sphere. The drag force \mathbf{F}_{f-s} , evaluated via Eq. 18, and the difference between the body force and the buoyancy force $\mathbf{F}_g = (0, 0, 0.1)^T$ acting on the sphere in Eq. 9 are used to update the particle velocity \mathbf{V}_p .

This simulation setup is well-suited for the verification of the fluid-solid coupling, because the geometry is simple and an analytical solution for the evolution and the terminal velocity of a sphere is available at various Reynolds numbers [21, 44]. From the particle Reynolds number $Re = 2|\mathbf{V}_p - \bar{\mathbf{u}}|R/\nu$ with ν the kinetic viscosity and $\bar{\mathbf{u}}$ the macroscopic flow velocity averaged over the whole lattice, the external body force \mathbf{F}_g balancing the drag force on the sphere can be computed analytically via

$$|\mathbf{F}_g| = |\mathbf{F}_{f-s}| = \frac{1}{2} C_d \pi R^2 \rho_f V_t^2, \quad \text{with} \quad C_d = 24/Re + 3.6/Re^{0.313} \quad (26)$$

where V_t is the terminal velocity and ν is only related to the relaxation time τ once the Δx and Δt are set. In what follows, the influence of the relaxation time τ on the terminal velocity of a single sphere will be investigated by varying τ from 0.6 to 2.0, which corresponds to $\nu \in (0.033, 0.5)$ in lattice unit.



(a) Drag, buoyancy and body forces acting on a settling sphere (b) Relative error of drag force over relaxation time τ

FIGURE 3 LBDEM simulation of a single sphere settling in viscous fluid.

The simulations run for a sufficient number of time steps in order to ensure that the sphere reaches its constant terminal velocity in each fluid. The number of time steps needed increases dramatically with the decrease of the relaxation time and the corresponding increase of the particle Reynolds number Re . After running for sufficient time, the saturated values of $|\mathbf{V}_p - \bar{\mathbf{u}}|$ approximate the terminal velocities V_t , and enter Eq. 26 for the calculation of the drag force acting on the sphere. The relative error of the drag force depending on the choice of the relaxation time is shown in Fig. 3b. The prediction errors given by the momentum exchange method are lower than 2% for $\tau \in (0.8, 1.8)$. The predicted drag force is seemingly independent of the relaxation time, especially in the intermediate Reynolds number regime, a feature particularly relevant for the simulation of waves in saturated granular media where the pore-scale squirt flow [15, 48, 49] plays an important role at high frequencies.

3.2 | Pressure wave in fluids and saturated granular media

The propagation of a plane wave in a viscous fluid is chosen as the first benchmark for the verification of the acoustic source, following [40, 41]. The 2D cross section at $x_2 = 6$ of the cubic fluid domain ($12 \times 12 \times 620$) is shown in Fig. 4a. The acoustic source is located on the left hand side ($x_3 = 1$), where a P-wave is agitated by a change in the local density with a sinusoidal waveform according to Eq. 25. The pressure at the opposite side ($x_3 = 620$) is locked to the equilibrium. The rest of the boundaries are periodic to mimic an infinite fluid between the two pressure boundaries. The boundary nodes have an off-equilibrium density magnitude of $\rho' = 1 \times 10^{-4}$, with the mean density $\rho_f = 1$, the angular frequency $\omega = 0.03$ and the number of the simulation steps $t_n = 5000$.

The other benchmarks consist in adding a granular chain of monodisperse spheres with an overlap of $\|\mathbf{u}_m\| = 0.01$ into representative volumes that have the same size as the cubic fluid domain aforementioned. The same acoustic source and boundary conditions as in the pure fluid are applied, except for the second benchmark in which a mechanically-induced impulse is used. As shown in Figs. 4b–4c, a total of 60 spheres are inserted one after another in the x_3 direction at $x_3 = i(2R - \|\mathbf{u}_m\|)$, $i = 1, 2, \dots, 60$, with x_1 and x_2 equal to 6. In the second benchmark (Fig. 4b), the solid spheres can move and interact, while the hydrodynamics (LBM) are switched off in order simulate elastic wave propagation in the same granular chain in dry condition. In this case, the first sphere is slightly shifted to the right at $x_3 = 10.001$, introducing a small perturbation between the first and the second sphere, which propagates an elastic wave. In the third and fourth benchmarks (Figs. 4c and 4d), the solid spheres are mobile and fixed in space, respectively, with the hydrodynamic interactions accounted for by the MEM. With the particle motions completely constrained, mechanical waves caused by collisions between the spheres are excluded. By doing so, the influence of the fluid-solid coupling and the mechanical interactions on the acoustic behavior of the pore fluid can be studied separately. In the cases where the spheres are allowed to move and interact, the interparticle forces in normal direction are governed by Eq. 11 with $E_p = 10$ and $\nu_p = 0.2$. The same relaxation time $\tau = 1.0$ is used in all benchmark simulations.

The propagation of elastic waves at different speeds is clearly observed from the snapshots of all physical systems at $t = 800$, as shown in Fig. 4. It can be seen that the acoustic attenuation in the x_3 direction differs as well, depending on the presence and the mobility of the solid spheres (see Figs. 4a and 4c and 4d). To quantify the propagation speed and attenuation in each saturated system, the off-equilibrium density ρ' within each cross section of the fluid domain perpendicular to the x_3 axis is averaged at each time step. Note that the average of ρ' runs only over the nodes which are not occupied by the solid spheres. The resulting evolution of the averaged ρ' in space and time is plotted for the pure fluid in Fig. 5a, the saturated chain of mobile particles in Fig. 5g and the saturated chain of fixed particles in Fig. 5j. For the dry granular chain, the elastic wave propagation can be understood from the evolution of the particle velocity in space and time, as shown in Fig. 5d.

The propagation of the averaged ρ' in the x_3 direction at $t = 800$ is extracted from Figs. 5a, 5d, 5g and 5j and plotted in Figs. 5b, 5e, 5h and 5k. Thanks to the acoustic sources that send the sinusoidal signals, the acoustic responses in the first, third and fourth benchmark cases can be described by the analytical stationary solution of the one-dimensional lossy wave equation, namely

$$\rho' = A \exp^{-\alpha_s x} \exp^{j(\omega t - kx)}, \quad \text{with} \quad \alpha_s = \frac{\omega}{c_s \sqrt{2}} \sqrt{\frac{\sqrt{1 + (\omega \tau_s)^2} - 1}{\sqrt{1 + (\omega \tau_s)^2}}}, \quad (27)$$

where A is a constant, k is the angular wavenumber, and τ_s is the relaxation time for acoustic attenuation $\tau_s = 2\nu/c_s^2$; α_s is the spatial absorption coefficient, which is negligible in low-frequency ranges but becomes more pronounced as the frequency increases. Note that τ_s is related to the relaxation time of the lattice BGK model (Eq. 4) via $\tau_s = 2(\tau - \Delta t/2)$. With the current choice of the time step $\Delta t = 1.0$ and relaxation time $\tau = 1.0$, τ_s is reduced to τ .

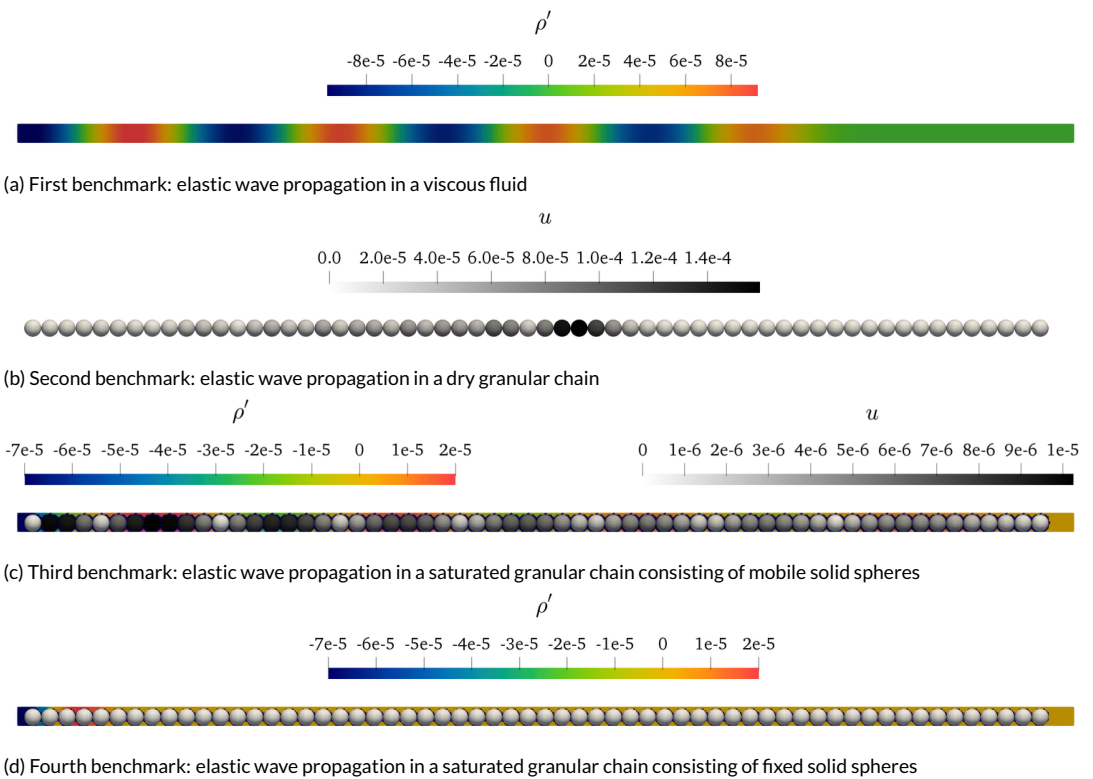


FIGURE 4 Snapshots of elastic waves propagating in different systems at $t = 800$. The pressure wave is agitated by a continuous sinusoidal signal with magnitude $\rho' = 1 \times 10^{-4}$ and frequency $\omega = 0.3$. See the Supplementary Material 1 for the animation.

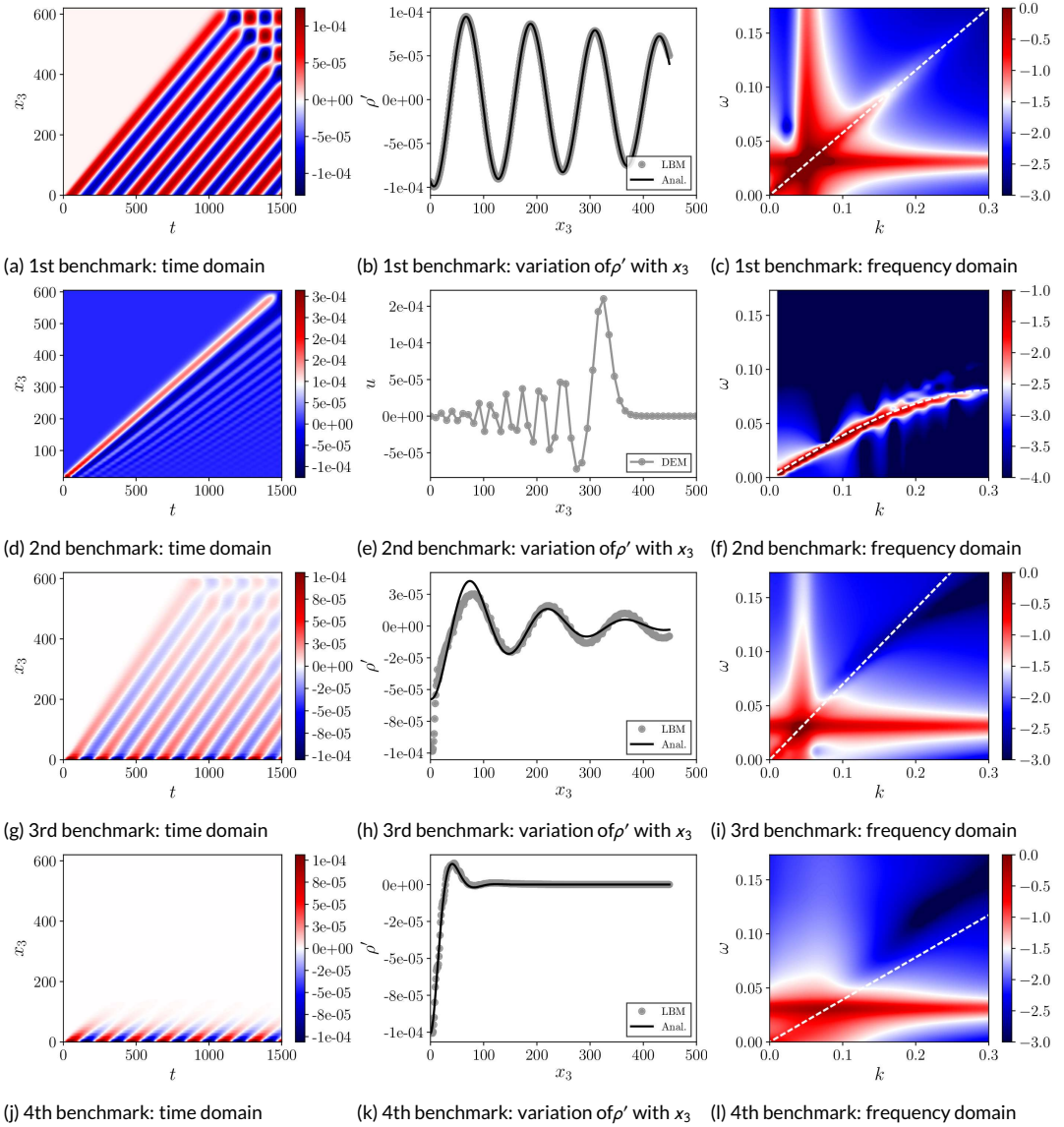


FIGURE 5 Elastic wave propagation in a pure fluid (a–c), a dry granular chain of mobile particles (d–f) and two saturated granular chains of mobile particles (g–i) and fixed particles (j–l). The acoustic sources in the first, third and fourth benchmarks emit sinusoidal waves, whereas the wave in the second benchmark is agitated by an impulse. The comparison between the evolutions of averaged off-equilibrium density ρ' in space and the analytical solutions is obtained at $t = 800$. The subplots (a,g,i) and (c,i,l) are colored by ρ' and the amplitude spectra of its discrete Fourier transforms respectively, in the logarithmic scale. The subplots (d) and (f) are colored by particle velocity u and the amplitude spectra of its discrete Fourier transform in the logarithmic scale.

For the pure fluid, the sound speed and the spatial absorption coefficient are known, i.e., $c_s = 1/\sqrt{3}$ and $\alpha_s = 7.79 \times 10^{-4}$, resulting from $\tau = 1.0$ and $\omega = 0.03$. The only fitting parameter in Eq. 27 is A which is determined from the variation of cross-section averaged ρ' from the source at $x_3 = 1$ to $x_3 = 450$ in Fig. 5b. By setting $\angle A^{\text{Re}}/\rho' = -0.023$ and $A^{\text{Im}}/\rho' = -1.003$, the behavior predicted by the LBM simulation correctly matches the analytical solution. With the acoustic source verified in the pure fluid, we now let c_s and α_s be the additional free parameters, in order to quantify the propagation speed and attenuation in the saturated granular chains. By fitting Eq. 27 with the acoustic responses in Figs. 5h and 5k, we obtain $A^{\text{Re}}/\rho' = -0.578$, $A^{\text{Im}}/\rho' = -0.117$, $\alpha_s = 6.627 \times 10^{-3}$ and $c_s = 0.698$ for the saturated granular chain of mobile particles, and $A^{\text{Re}}/\rho' = -1.22$, $A^{\text{Im}}/\rho' = -0.236$, $\alpha_s = 4.819 \times 10^{-2}$ and $c_s = 0.391$ for the saturated granular chain of fixed particles. The different values of c_s and α_s show that when the constituent particles are allowed to interact elastically, the wave undergoes much less attenuation in the saturated system and the sound speed is almost doubled.

The discrete Fourier transform (DFT) of the space-time domain data gives the dispersion relations of the single/two-phase systems, as shown in Figs. 5c, 5f, 5i and 5l. From the straight lines that cross the inserted frequency and the most significantly agitated wavenumbers (white broken lines), the sound speeds are obtained, e.g., the lattice speed of sound is recovered from Fig. 5c that is $c_s \approx 1/\sqrt{3}$, which proves that the acoustic wave is propagated with the accurate speed in the pure fluid. Note that the slopes agree well with the sound speeds fitted with Eq. 27. Interestingly, the dispersion relation of the dry granular chain in Fig. 5f is highly nonlinear, because of the interparticle collisions that give rise to the frequency dependence. It appears that the nonlinear dispersion relation of the dry granular chain is completely suppressed by the coupled motion of the pore fluid and the hydrodynamic interactions, as shown in Fig. 5i. The sound speed therein is higher than both in the pure fluid and the dry granular chain. We will discuss this point further in Sec. 5. By constraining the degrees of freedom of all solid particles (see Fig. 5j, 5k, 5l) while allowing a flow in the pore space, the speed of sound is significantly decreased, as can be seen by comparing Fig. 5g and 5j. This is because the path along which the acoustic wave propagates in the pore fluid until time t is always longer than the travel distance. In addition, when the solid phase is rigid, the only attenuation mechanism is the pore-scale fluid flow. When the solid particles are allowed for elastic interactions, the attenuation becomes less pronounced, because of the in-phase motion of the solid particles and the pore fluid. Nevertheless, the acoustic attenuation in the pure fluid is much weaker than in the dry/saturated granular chains, as indicated by the fitted spatial absorption coefficients and shown in Fig. 5d, 5g and 5j.

4 | MODELING ELASTIC WAVE PROPAGATION IN ORDERED, SATURATED GRANULAR MEDIA

As envisaged by Biot [31], the simplest setup to evaluate, the so-called *viscodynamic* operator, is a face-centered-cubic (FCC) packing of equally-sized spheres, pushed by an alternating motion from the fluid as illustrated in Fig. 6. The ordered FCC packing is apparently more complicated than the particle chains in Sec. 3.2. However, the elastic wave speeds of such ordered granular packings can be computed analytically in dry conditions by means of the effective medium theory. In order to reproduce the propagation of waves in saturated granular media, the discretization parameters are selected so as to meet the true sound speed in water. With this, the influence of acoustic sources and effective confining pressure are investigated as well.

4.1 | Face-centered cubic packing of frictionless spheres

In a similar fashion as the benchmarks in Sec. 3.2, the oscillating pressure boundary condition is applied on the left hand side ($x_3 = 1C_I$) of the fluid domain ($40C_I \times 40C_I \times 1280C_I$), while a constant pressure is maintained on the right hand side. The other boundary conditions are assigned to be periodic in order to mimic an infinitely large, homogeneous and fully saturated packing. Within the cubic fluid domain, a $4 \times 4 \times 200$ FCC packing of equally-sized frictionless spheres is inserted. Note that the same configuration was adopted by [14] for DEM modeling of wave propagation in dry granular media. The leftmost and rightmost layers of solid spheres are fixed in space, so that effective stresses on the FCC packing are kept constant. The radius of each sphere is set to $R = R_0 + 0.5|u_n|$; $R_0 = 5C_I$ is the radius that leaves zero overlap between the spheres in the FCC packing and $|u_n|$ is the overlap that gives rise to the effective stress.

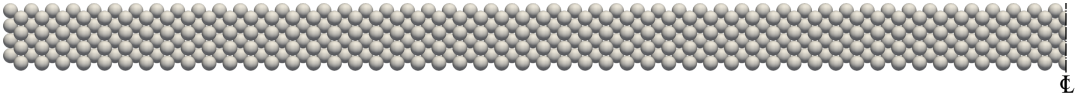


FIGURE 6 A fully saturated regular face-centered-cubic packing of spherical particles.

4.2 | Model parameters and numerical aspects

Setting the model parameters of LB-DEM simulations can be difficult, especially for the application to wave propagation in poroelastic media. Relevant physical parameters need to be properly selected to reproduce both the flow and acoustic behaviors. The kinematic viscosity ν depends on the choice of the spatial and temporal resolutions and a single model parameter τ . For the computational Mach number M to be sufficiently small, the lattice speed of sound c_s is tuned to be much larger than the maximum flow velocity $|u_{max}|$ via Δx and Δt . For LBM simulations of fluid flow, M is typically smaller than 0.1, meaning that c_s is not necessarily the true sound speed of the fluid. One can choose a preferred spatial resolution Δx and then τ for the target viscosity, which in turn gives the corresponding value for Δt . However, this is not the case for LB-DEM modeling of elastic waves. First, c_s has to be chosen equal to the true sound speed in the fluid (e.g., $c_s = 1500$ m/s for water), leaving ν dependent on τ and Δx , that is $\nu = \tau c_s^2 - \sqrt{3}c_s \Delta x/6$. Second, for the LB-DEM simulations to be numerically stable, the BGK collision operator requires τ to be larger than 0.5. As a consequence, to match the kinematic viscosity of water, $\nu = 10^{-6}$ m²/s, with the smallest allowable relaxation time $\tau = 0.5$, the spatial resolution Δx would have to be 2.598 km which is obviously beyond the scale of micromechanics. If one wants to use the length scale of a typical solid particle, for example $\Delta x = 10^{-3}$ m, the resultant τ then is as small as 1.92×10^{-7} . Therefore, in this work we choose to only match the sound speed of water rather than the viscosity. Ongoing work involves the implementation of a regularized LBM to reduce the lower limit of the relaxation time (not shown here).

For the following LB-DEM simulations of wave propagation in saturated granular media, we use the parameters in Table 1 listed in both dimensionless and dimensional units. The LBM and DEM calculation cycles share the same time step Δt . In order to investigate the effect of the acoustic source on the simulation results, a variety of input waveforms and frequencies are considered (see Table 2). In contrast to the granular chains subjected to continuous signals in Sec. 3.2, the elastic wave in each LB-DEM simulation is agitated by a single period pulse. Different values for the overlap $|u_n|$ between solid spheres are selected, such that the effective confining pressure on the FCC packing varies from 0.1 MPa to 30 MPa.

Fig. 7 shows snapshots of a typical LB-DEM simulation of wave propagation in a FCC packing of spheres. The pressure wave is agitated by a cosine signal with the magnitude of the off-equilibrium density $\rho' = 0.33$ (kg/m³) at an

TABLE 1 Model parameters for LB-DEM modeling of elastic wave propagation in saturated granular media.

Parameters	Dimensionless units		Dimensional units	
Length	Δx^*	1	Δx	0.004 mm
Time	Δt^*	1	Δt	1.54×10^{-6} ms
Speed of sound	c_s^*	$1/\sqrt{3}$	c_s	1500 mm/ms
Pressure	p^*	1/3	p	2.25 GPa
Velocity	u^*	1	u	2598 mm/ms
Density (fluid)	ρ_f^*	1	ρ_f	10^3 kg/m ³
Relaxation time	τ^*	1	ν	1.732 mm/ms ³
Density (solid)	ρ_p^*	2.466	ρ_p	2.466×10^3 kg/m ³
Young's modulus	E_p^*	10.37	E_p	70 GPa
Poisson's ratio	ν_p^*	0.2	ν_p	0.2
Interparticle friction	μ^*	0	μ	0

The lengthscale and timescale conversion factors are: $C_l = 0.004$ mm and $C_t = 1.54 \times 10^{-6}$ ms.

TABLE 2 Different input waveforms and frequencies used by the oscillating pressure boundary.

Frequency (MHz)	Waveform ($t \leq t_n \Delta t$)	ρ' magnitude (kg/m ³)
6.50	Step: $\rho = \rho_f + \rho'$	0.2
6.50	Cosine: $\rho = \rho_f + \rho'(1 - \cos(\omega t))$	0.2
6.50	Sine: $\rho = \rho_f + \rho' \sin(\omega t)$	0.2
1.30	Cosine: $\rho = \rho_f + \rho'(1 - \cos(\omega t))$	0.2
3.25	Cosine: $\rho = \rho_f + \rho'(1 - \cos(\omega t))$	0.2
13.0	Cosine: $\rho = \rho_f + \rho'(1 - \cos(\omega t))$	0.2

input frequency of 1.30 MHz. Similar to the averaged off-equilibrium density ρ' in Sec. 3.2, the macroscopic momentum $\bar{\rho}\bar{u} = \sum \rho u / \sum \rho$ is averaged within each cross section. Note that within the solid spheres, both $|u|$ and ρ are zero. Applying the DFT to the evolution of $\bar{\rho}\bar{u}_3$ in time and the propagation direction x_3 , gives the P-wave dispersion relation of the pore fluid. Similarly, the dispersion relation of the other phase, i.e., the solid FCC packing, can be obtained from the particle velocity vectors V_p . In particular, the components of V_p along x_3 and perpendicular to x_3 provide the P- and S-wave dispersion relations of the solid phase.

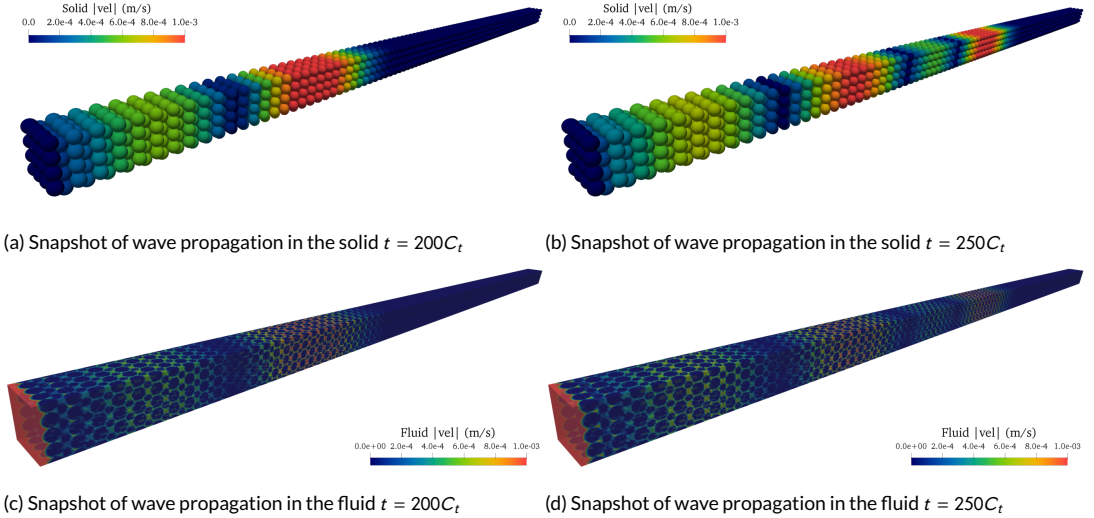


FIGURE 7 Snapshots of elastic wave propagation in a saturated FCC packing of solid spheres, agitated by a cosine signal with the magnitude of $\rho' = 0.33 \text{ kg/m}^3$ and the frequency $\omega/(2\pi) = 1.30 \text{ MHz}$. See the Supplementary Material 2 for the animation.

4.3 | Comparison of wave propagation in dry and saturated FCC packings

4.3.1 | Mechanically agitated impulse

The acoustic source at the pressure boundary aims to simulate the propagation of acoustic waves from a viscous fluid to a saturated granular medium. With this acoustic source, the input waveform, the input frequency and the elapsed time of a periodic pulse can be freely controlled. Alternatively, the wave can be agitated by perturbing the solid phase at a given position, with an initial overlap slightly bigger than the overlaps elsewhere [11, 50, 51], e.g., between the boundary particles fixed in space and their neighbors. The resulting unbalanced forces on the neighboring spheres in turn induce an impulse propagating into the granular packing. If the unbalanced forces are aligned with the propagation direction, a P-wave will be agitated, otherwise a shear wave (S-wave) will be triggered. This mechanically agitated impulse is well-suited for DEM modeling of wave propagation in dry granular materials. However, it can cause strong oscillations in the pore fluid when the mechanical pulse couples with the LBM. Thus, for saturated granular materials, an acoustic source embedded in the fluid phase (see Sec. 2.4) appears to be preferable. However, in order to compare the acoustic behavior of dry and saturated granular packings, the mechanical agitated impulse is used.

4.3.2 | Time domain and frequency domain responses

To understand the effect of pore fluids on the dispersion relations of granular media, the acoustic responses of the dry and saturated FCC packings under an effective confining pressure of 5 MPa are compared. The elastic waves in both cases are agitated by perturbed overlaps initially set in the leftmost layer of solid spheres ($x_3 = 2C_f$), pointing towards the propagation direction x_3 . Following the same averaging scheme as in Sec. 4.2, the time-domain and the frequency-domain responses of the saturated and dry FCC packings are obtained and plotted in Figs. 8 and 9.

It can be observed from the space time signal in Fig. 8a that the main pulse broadens as the wave travels through the saturated FCC packing, before it is reflected. Interestingly, there exists another wave which is located almost close to the source ($x_3 = 2C_f$). This wave is slow and highly dissipative, and has features of the slow P-wave predicted by Biot [31]. Fig. 8b shows the amplitude spectrum of the time-domain signal of the averaged fluid momentum. The dispersion relation, that is the relationship between wavenumber k and frequency ω , appears to be almost linear.

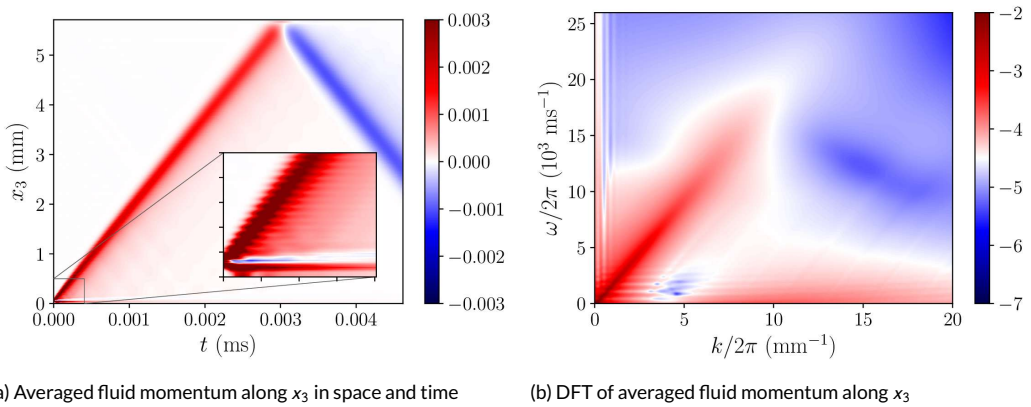


FIGURE 8 Time-domain and frequency-domain responses of the saturated FCC packing agitated by an impulse signal resulting from the initial perturbation at the left boundary. The color bar in (a) shows the time-domain response in m/s and in (b) the amplitude spectrum of its discrete Fourier transform in the logarithmic scale.

For the dry FCC packing, the dispersion relations are highly nonlinear, i.e., the wave velocity decreases with the increase of the wavenumber and the frequency [14, 13]. The group velocity approaches zero in the very high frequency regime, as shown in Fig. 9a. The amplitude spectrum of the particle velocity components along x_3 in Fig. 9c highlights the P-wave dispersion relation of the saturated FCC packing, which is identical to the one for the pore fluid (see Fig. 8b). This proves that the in-phase motions of the pore fluid and the submerged solid spheres indeed causes the propagation of P-waves in saturated granular media. By comparing Figs. 9a and 9c, one can find that the fluid-solid coupling qualitatively changes the P-wave dispersion relation of the FCC packing. It is known that the P- and S-waves are decoupled for regular crystalline structures like the FCC configuration, i.e., no shear wave is induced by P-wave propagation and vice versa. Therefore, it is not surprising that no S-wave branches are present in Fig. 9b. In the case of the saturated packing, however, the S-wave branch appears in the amplitude spectrum (Fig. 9d) and is quite linear in the low frequency regime. Nevertheless, the S-wave is significantly more dissipative and dispersive than the P-wave, as can be observed from the much smaller Fourier amplitudes in 9d. A few inclined branches which have the same slope as the P-wave dispersion relation also enter the frequency domain in Fig. 9d. These weak branches are caused by fluctuations due to frequently updated fluid-solid links (see Fig. 2) due to strong longitudinal motions of the solid particles.

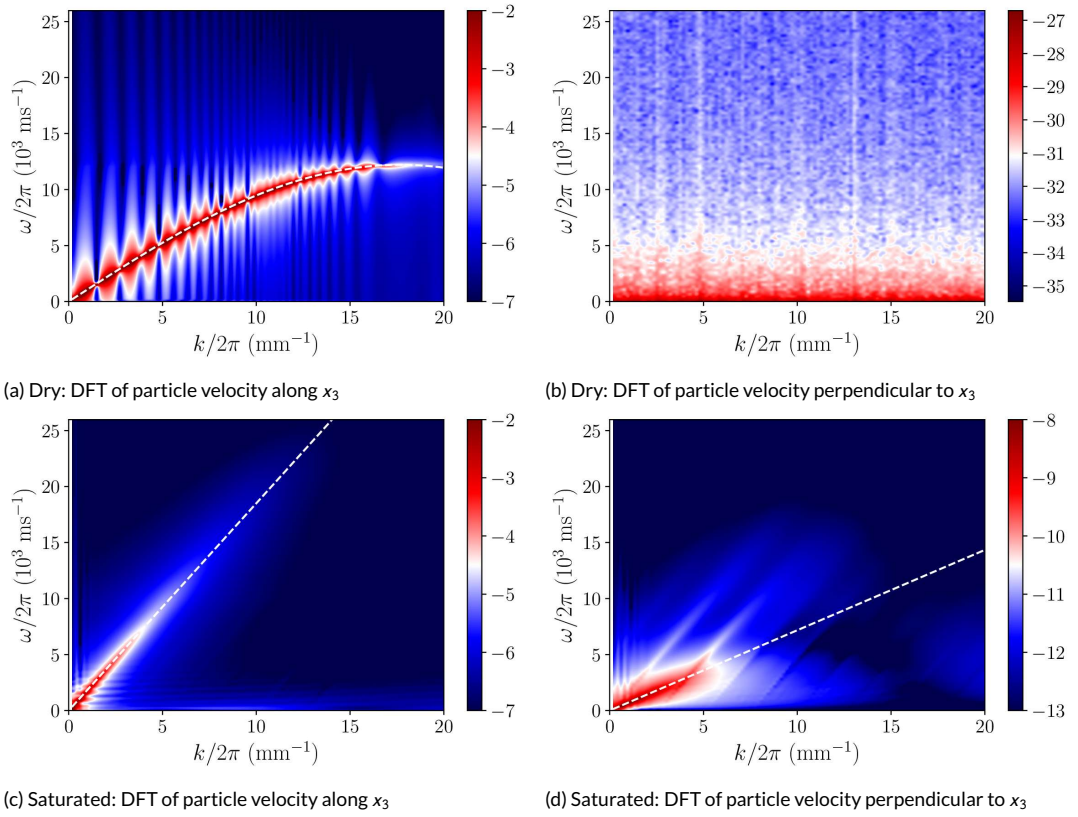


FIGURE 9 Frequency-domain responses of the saturated (a, b) and dry (c, d) FCC packings agitated by an impulse signal resulting from the initial perturbations at the left boundary. Note the much smaller amplitude in (b) and (d).

4.4 | Effect of acoustic source

Unlike typical ultrasonic experiments in which wave velocities are interpreted from the time evolution of signals, numerical simulations allow for direct measurements of wave velocities from dispersion branches in the frequency domain [14, 13]. For dry granular materials, it is known that input frequencies affect the identification of travel time and travel distance from received signals, and in turn, wave velocities. Therefore, the wave velocities derived from dispersion branches, obtained from simulations, can be treated as the “ground truth”. In this subsection, we investigate the effect of input waveforms and frequencies on the “ground truth” for saturated granular materials. The goal is to obtain clear dispersion branches so as to reproduce the dependence of the P- and S-wave velocities on the effective confining pressure, as predicted by the Biot’s theory.

4.4.1 | Effect of input waveform

Three waveforms, namely, single-period step, cosine and sine functions are tested in order to study the effect of input waveforms on the acoustic response of saturated granular media (see Table 2 and Fig. 10. Figs. 11a, 11d and 11g show the evolution of the cross-section averaged momentum $\rho \bar{u}_3$ in time and space, in response to the step, cosine and sine signals. In the case of square signal, the local momentum shows sharp increase near the source that stays almost constant in the remaining time, as shown in Fig. 11a. Differently, in the case of a cosine signal, a single peak is inserted (see Fig. 11d. The cosine function also guarantees a smooth transition of local densities at the source from equilibrium to non-equilibrium and then back to equilibrium during $t \leq t_n \Delta t$. The sine signal, however, inserts a peak and a trough of equal magnitudes, and the wavelengths of the two resulting signals are not broadened during the propagation, as shown in Fig. 11g. It appears that the sinusoidal signal is dissipated more significantly along the propagation distance than the other signals.

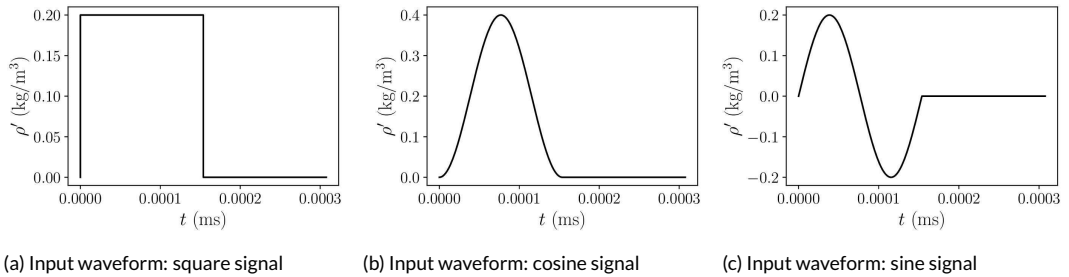


FIGURE 10 Three single-period input signals used by the acoustic source.

Similar to Figs. 9c and 9d, Figs. 11b, 11e, 11h and Figs. 11c, 11f, 11i show the P- and S-wave dispersion branches for the respective input waveforms. Compared with the sine signal, both the square and the cosine signals activate the P-wave dispersion relations in the low-wavenumber range, as shown in Figs. 11b and 11e. The P-wave dispersion relation in Fig. 11h is more pronounced in the high-frequency range ($\omega/2\pi > 2$ MHz), which is associated with the less broadened signals in Fig. 11g. Regardless of the difference in the amplitude spectrum, the slopes of all dispersion branches are seemingly identical. Interestingly, a few frequency bands seem to be more or less active for the different inserted signals. While frequency bands caused by the sine and cosine signals are consistent, the square signal creates low-intensity frequency bands with equal intervals, but activates higher frequencies as well. Similar features can be observed in the S-wave dispersion relations as shown in Figs. 11c–11i. Apparently, the transverse motions of the solid

particles induced by the square and cosine signals of the pressure wave are stronger than those induced by the sine signal. The intensity on the S-wave dispersion branch in Fig. 11f is comparable to the noise induced by the P-wave, making it difficult to accurately identify the slope, as shown in Fig. 11i. The P- and S-wave dispersion branches in Fig. 11e and 11f are less interrupted by the low-intensity frequency bands, which leads more accurate estimates of the wave velocities. Therefore, we use the cosine waveform in the following sections, although the dispersion relations in the low-frequency ranges are clear for both the square and cosine signals.

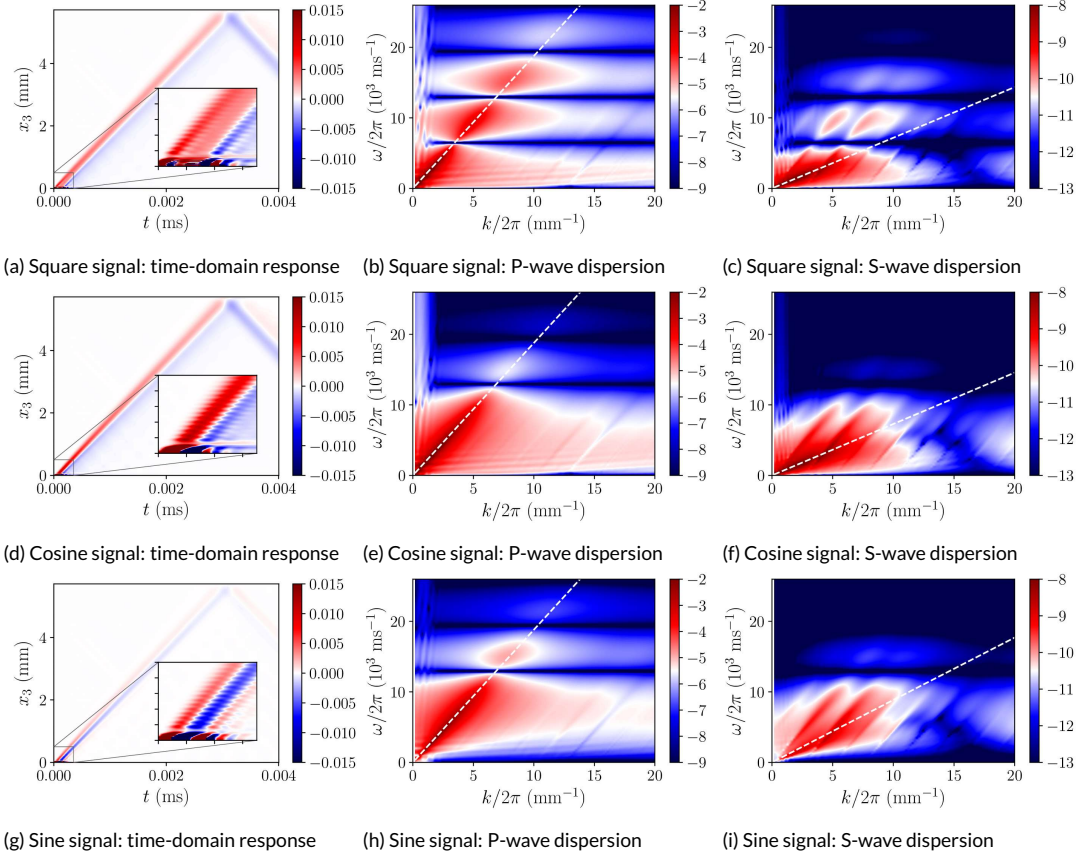


FIGURE 11 Time-domain and frequency-domain responses of the saturated FCC packing, agitated respectively by a square signal (a–c), a cosine signal (d–f) and a sine signal (g–i) sent from the oscillating pressure boundary. Color code indicates the amplitude of the particle velocity components in the longitudinal direction (b, e and h) and the transverse direction (c, f and i).

4.4.2 | Effect of input frequency

Using the cosine waveform and the input frequencies given in Table 2, the P-wave and resulting S-wave dispersion relations are obtained for three different input frequencies. The space-time evolution of the longitudinal particle velocity is plotted in Figs. 12a–12g, and the P-wave and S-wave dispersion branches in Figs. 12b–12h and Figs. 12c–12i,

for the respective input frequencies. Pulse broadening can be observed in Fig. 12a, i.e., the high-frequency signals decay rapidly as the wave propagates in time and space. With decreasing input frequency, the pulse broadening phenomenon becomes less pronounced as shown in Figs. 12d and 12g, which reflects the dispersive nature of the waves in granular media. As the input frequency decreases, the dispersion relation becomes clearer at the frequencies smaller than approximately twice as large as the input value (1.30, 3.25 and 13.0 MHz in Figs. 12h, 12e and 12b, respectively). Nevertheless, the dispersion relation is already very weak at the input frequency of 13.0 MHz, as shown in Fig. 12b. In contrast to the dispersion relation of dry granular media in Fig. 9a, the largest Fourier coefficients always appear in the low-frequency ranges, which are associated with the frequency bands activated by the input frequency.

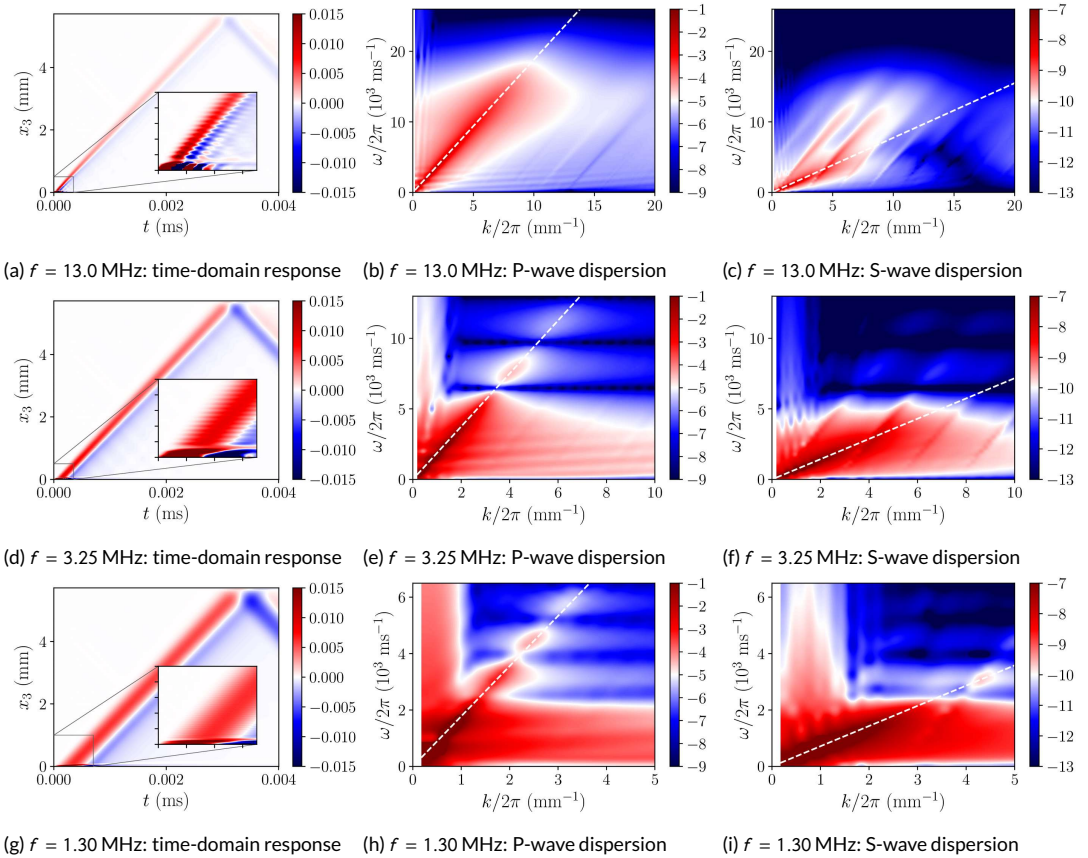


FIGURE 12 Time-domain and frequency-domain responses of the saturated FCC packing, agitated respectively by cosine signals at input frequencies ($f = \omega/2\pi$) of 13.0 MHz (a–c), 3.25 MHz (d–f) and 1.33 MHz (g–i) sent from the oscillating pressure boundary. Color code indicates the amplitude of the particle velocity components in the longitudinal direction (b, e and h) and the transverse direction (c, f and i).

The noisy branches in Fig. 12c and 12f that resemble the P-wave dispersion relation are caused by the longitudinal motion of the particles. Using low input frequencies, e.g., $f = 1.30$ MHz at the acoustic source, the noisy signals in the amplitude spectrum of the S-waves are reduced, as shown in Fig. 12i. Note that the S-wave dispersion relations here are obtained with the transverse velocity components of the solid particles. Although not shown here, only the

P-wave dispersion branch is obtained from the DFT of the cross-section averaged fluid momentum in the transverse direction $\rho\bar{u}_3$. This is reasonable, because the pore fluid cannot sustain shear. Irrespective of the input frequencies, clear dispersion relations can be identified, which are consistently linear for both the P- and S-waves. In order to accurately fit each dispersion relation with a straight line, a large number of relevant data points in the frequency domain is needed. Therefore, we select an input frequency of 13.0 MHz for the following LB-DEM simulations at various effective confining pressures, while keeping a sufficient number of time steps during which the acoustic source remains active for a single period.

5 | WAVE VELOCITIES FROM THE HYDRO-MICROMECHANICAL MODEL AND BIOT'S THEORY

Biot [31] derived theoretical equations for predicting the velocities of a fully saturated poroelastic material given the elastic constants of the dry solid matrix and the characteristics of the fluid. Biot's theory incorporates the governing mechanisms such as viscous and inertial interaction between the pore fluid and the solid matrix. The present hydro-micromechanical model is capable of numerically reproducing the relevant mechanisms in the poroelastic medium, i.e., granular interactions, fluid-solid coupling and pore-scale fluid flow in detail. Therefore, the theory of poroelasticity of Biot is well-suited for the validation of the present model. The goal here is twofold. First, the numerical and analytical predictions are compared. Second, results from the direct simulations are analyzed to investigate the characteristic features predicted by Biot's theory.

The system chosen is the same FCC packing of monodisperse spheres as in Sec. 4. In order to reproduce the pressure dependence of wave velocities in saturated granular media, a wide range of overlaps between the solid spheres are considered, such that the macroscopic effective confining pressure ranges from 0.1 MPa to 30 MPa. The same model parameters in Table 1, as for the studies on input waveforms and frequencies in Sec. 4.4, are adopted here. Given the discussions in Sec. 4.4, a single-period cosine signal at an input frequency of 13.0 MHz is used by the acoustic source, at various levels of effective stress.

5.1 | Dispersion relations at various effective confining pressures

In Fig. 13, we show the variation of the P- and S-wave dispersion relation with increasing effective stress. As expected, the tangents to both dispersion branches increase with elevated effective confining pressure. The fitted P-wave dispersion curves (white broken lines) obtained from the macroscopic momentum in the pore fluid at effective confining pressures $p' = 0.1, 1.6, \text{ and } 30 \text{ MPa}$ are given in Figs. 13a, 13d and 13g, and appear to be identical to the ones in Figs. 13b, 13e and 13h of the solid phase. This confirms again that P-waves in the pore fluid and in the assembly of solid spheres travel with the same wave velocities. In contrast to the exact same dispersion branches in Figs. 8b and 9c, wide horizontal bands appear approximately around the input frequency ($f = 13.0 \text{ MHz}$) and merge with the P-wave dispersion branches in all amplitude spectra of the pore fluid (Figs. 13a, 13d and 13g). Nevertheless, the wide horizontal bands are not present in the amplitude spectra of the solid phase (Figs. 13b, 13e and 13h). The wide horizontal bands are possibly caused by the input frequency inserted from the acoustic source in the fluid domain. Figs. 13c, 13f and 13i show the S-wave dispersion branches induced by the coexisting P-waves at $p' = 0.1, 1.6 \text{ and } 30 \text{ MPa}$. The pressure dependence of the S-wave velocities is more evident than that of the P-wave. Since the pore fluid does significantly affect the propagation of S-waves, the dependence of S-waves on pressure strongly resemble that in dry granular materials.

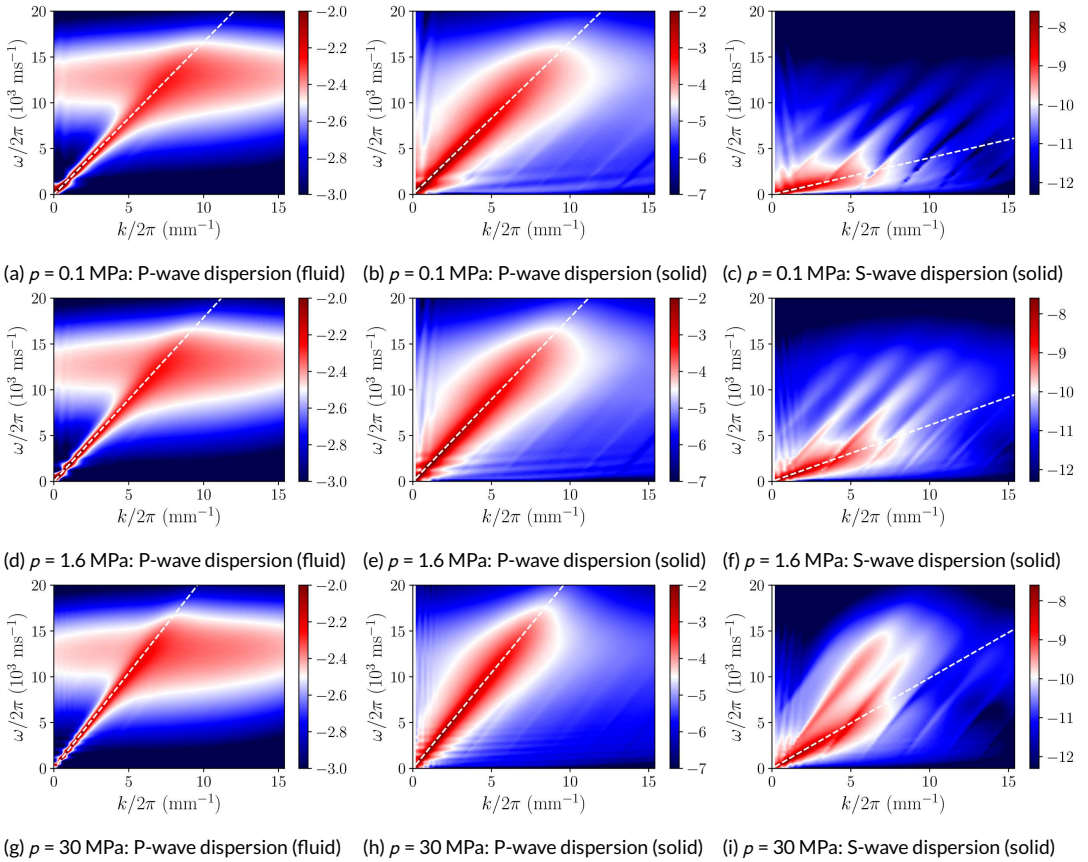


FIGURE 13 Time-domain and frequency-domain responses of the saturated FCC packings agitated by a cosine signal sent from the oscillating pressure boundary, at various effective confining pressures $\rho = 0.1$ MPa (a–c), 1.6 MPa (d–f) and 30 MPa (g–i). Color code indicates the amplitude of the particle velocity components in the longitudinal direction (b, e and h) and the transverse direction (c, f and i). Color code indicates the amplitude of the particle velocity components in the longitudinal direction (a, b, d, e, g and h) and the transverse direction (c, f and i).

5.2 | Biot's equations of wave velocities in saturated poroelastic media

Biot's theory predicts the wave velocities in saturated poroelastic materials at high frequencies, depending on the elastic properties and densities of the constituent solid matrix and pore fluid (see Table 1. From the microstructure and the Young's modulus E_p and Poisson's ratio ν_p of the solid particles, the pressure-dependent bulk and shear moduli of the dry FCC packing, K_{dry} and G_{dry} , are predicted by the effective medium theory [52]. Knowing K_{dry} and G_{dry} , the porosity ϕ , the bulk modulus of the solid particles K_p from E_p and ν_p , the bulk modulus of the pore fluid K_f from the sound speed in the fluid c_s , and the solid and fluid densities ρ_p and ρ_f , the wave velocities of the saturated FCC packing are given by

$$v_p(\text{fast, slow}) = \sqrt{\frac{\Delta \pm \sqrt{\Delta^2 - 4(\rho_{11}\rho_{22} - \rho_{12}^2)(PR - Q^2)}}{2(\rho_{12}\rho_{22} - \rho_{12}^2)}}, \quad (28)$$

$$v_s = \sqrt{\frac{G_{dry}}{\hat{\rho} - \phi\rho_f\alpha^{-1}}}, \quad (29)$$

$$\Delta = P\rho_{22} + R\rho_{11} - 2Q\rho_{12}, \quad (30)$$

$$\rho_{11} = (1 - \phi)\rho_p - (1 - \alpha)\phi\rho_f, \quad \rho_{22} = \alpha\phi\rho_f \quad \text{and} \quad \rho_{12} = (1 - \alpha)\phi\rho_f, \quad (31)$$

$$\hat{\rho} = (1 - \phi)\rho_p + \phi\rho_f, \quad (32)$$

where K_{dry} and G_{dry} are the pressure-dependent bulk and shear moduli of the dry FCC packing, ρ_{11} and ρ_{22} are the effective mass of the solid matrix and the fluid, incorporating the induced mass ρ_{12} caused by inertia drag that arises from the relative acceleration between the solid particles and the pore fluid, $\hat{\rho}$ is the total apparent mass of the saturated FCC packing with the tortuosity parameter $\alpha = 1 - r(1 - 1/\phi)$ ($r = 0.5$ for spheres), P , Q and R are the elastic moduli defined as

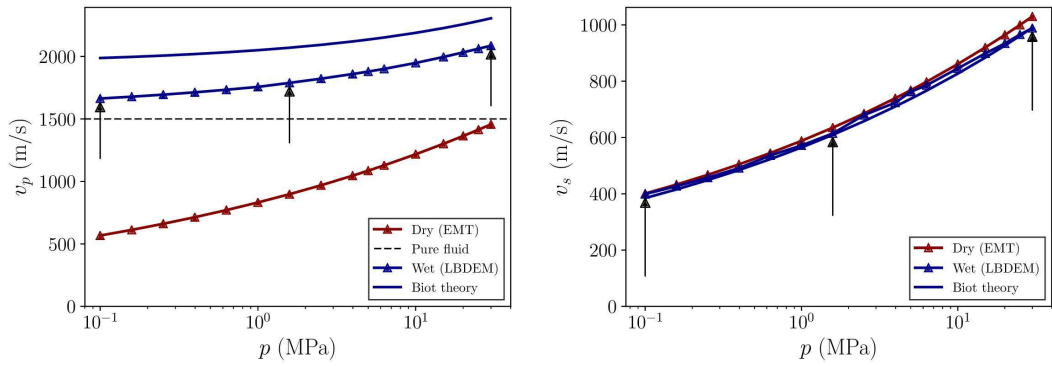
$$P = \frac{(1 - \phi)(1 - \phi - K_{dry}/K_p)K_p + \phi K_p K_{dry}/K_f}{1 - \phi - K_{dry}/K_p + \phi K_p/K_f} + \frac{4}{3}G_{dry}, \quad (33)$$

$$Q = \frac{(1 - \phi - K_{dry}/K_p)\phi K_p}{1 - \phi - K_{dry}/K_p + \phi K_p/K_f}, \quad (34)$$

$$R = \frac{\phi^2 K_p}{1 - \phi - K_{dry}/K_p + \phi K_p/K_f}. \quad (35)$$

The two solutions of v_p given in Eq. 28 correspond to the fast and slow P-waves. The fast P-wave can be easily measured in both the laboratory and the field, and it reflects the in-phase motion between the solid matrix and the pore fluid. As shown in Eq. 28, Biot's theory predicts a secondary slow P-wave slow P-wave, which is highly dissipative resulting from the overall out-of-phase motion between the solid and the fluid. The S-wave velocity v_s given in Eq. 29 incorporates an inertia coupling term which modifies G_{dry} with the apparent mass and the geometry of the packing.

From the P- and S-wave dispersion relations in Fig. 13 (see the Supplementary Material 3 for the amplitude spectra at other effective confining pressures), the wave velocities from the hydro-micromechanical model are obtained. The numerical predictions and the analytical solutions given by Biot's theory are compared in Fig. 14. As predicted by Biot's theory, the in-phase motion of the pore fluid flow and the FCC packing of solid spheres leads to higher P-wave velocities compared with those of the dry packing. On the other hand, the inertia drag between the particles and the surrounding pore fluid increases the effective mass of the solid phase and thereby reduces the S-wave velocities. Both phenomena are qualitatively reproduced covering the pressure dependence, as shown in Figs. 14a and 14b. As the



(a) Compressional wave velocity versus pressure

(b) Shear wave velocity versus pressure

FIGURE 14 Comparison of wave velocities of the saturated FCC packing as predicted by the hydro-micromechanical model and Biot's theory at various effective confining pressures. Arrows refer to the three cases in Figs. 13a–13c, 13d–13f and 13g–13i.

effective confining pressure increases from 0.1 MPa to 30 MPa, the relative error between the analytical solution and the LB-DEM prediction of the P-wave velocity decreases from 19.49% to 10.53%, whereas the relative error for the S-wave velocity drops from 3.52% to 0.15%. It is not surprising that the analytical solutions of Biot do not match perfectly with the LB-DEM simulation results. The reason for the mismatch is expected, as some mechanisms are accounted for by the theory, e.g., viscous losses within the pore fluid and pore-scale squirt flow. In addition, the FCC packing of solid spheres is weakly anisotropic, because of the non-periodic boundaries on the left and right (see Sec. 4.1.

5.3 | Numerical evidence of the slow compressional wave

With the help of the coupled LB-DEM, not only the pressure-dependent dispersion relations can be obtained, but mechanisms like slow-wave diffusion can be investigated as well. The weakly inclined dispersion branches in Figs. 9c, 11b–11e and 12b–12h suggest the existence of the slow, dissipative P-wave propagation, irrespective of the difference in the acoustic source (e.g., perturbation in fluid/solid, waveforms and frequencies). As shown in the space-time evolution in the insets of Figs. 8a, 11a–11d and 12a–12g, there seems to be highly dissipative P-waves that propagate slowly from the acoustic source. The aforementioned weakly inclined branches are associated with the slow P-waves. As the confining pressure increases, the number of the weakly inclined bands increases with decreasing bandwidths, as shown in Figs. 13b, 13e and 13h. For better observation of the slow waves, the propagation of the locally averaged fluid momentum $\rho\bar{u}_3$ along the x_3 direction at various times are plotted for the step, cosine and sine waveforms in Fig. 15. The lags between the $\rho\bar{u}_3$ signals at various times give the P-wave velocities directly.

All subplots of Fig. 15 show the propagation of the fast P-waves indicated by the wavefronts on the right hand side. From Figs. 15a, 15b and 15c, the peaks relevant to the slow P-wave can be observed near the source, most clearly from the ones given by the cosine input signals. Although the signals agitated with the square waveform are noisy and contain high frequency contributions (coda), as shown in Fig. 15a, the peaks and troughs therein are seemingly correlated in time, which suggests the presence of the slow P-wave. With the sinusoidal waveform, the attenuation is so significant that the signals near the source are hardly noticeable. From Figs. 15a, 15b and 15c, it is confirmed again that the cosine waveform is best suited to agitate pressure waves from the fluid phase.

Similar to Sec. 4.4.2, the effect of input frequencies on the slow P-waves is investigated and shown in Figs. 15d, 15e and 15f. With decreasing input frequency, the existence of the slow P-wave becomes more evident. However, the travel distances and the wave velocities of the slow P-waves at different time steps cannot be measured, because of the slowness and high diffusivity of the waves.

The propagation of $\rho\bar{u}_3$ at different time steps along the x_3 direction associated with the influence of effective confining pressure are plotted in Figs. 15g, 15h and 15i, respectively. In addition to the increasing fast P-wave velocity, the slow P-wave becomes more dissipative as the effective confining pressure increases, which can be seen from the increasingly vanishing peaks relevant to the slow P-waves at $t = 10^{-3.8}$ ms. The enhanced dissipation may be attributed to the increasing natural frequencies of the FCC packing and the slightly enlarged overlap needed for the elevated effective confining pressure.

To accurately calculate the slow P-wave velocities, two numerical difficulties need to be properly tackled: first, the lower limit of the relaxation time has to be overcome so that LBM modeling of wave propagation in fluids with low viscosities become possible; second, the computation size at least along the propagation direction has to be sufficiently large so as to allow the slow P-wave to propagate with noticeable travel distances before reflections overlap. Ongoing work aims to overcome the current lower limit of the relaxation time with the regularized scheme of the LBM.

6 | CONCLUSIONS

A hydro-micromechanical model is proposed to simulate elastic wave propagation in saturated poroelastic granular media. The hydrodynamics in the pore fluid is resolved with the lattice Boltzmann method and the translational and rotational motion of solid particles are tracked with the discrete element method. The novelty lies in the effective fluid-solid coupling scheme, the oscillating pressure boundary condition and the benchmarks for wave propagation simulations. The fluid-solid coupling scheme is verified against the terminal velocities of a single sphere settling in viscous fluids at various Reynolds numbers. The relative errors are less than 2% for intermediate Reynolds numbers and the accuracy is found to be independent of the choice of the relaxation time. The oscillating pressure boundary is applied to a pure fluid and two saturated granular media with granular chains fixed and allowed to move in space. The acoustic responses are compared with one-dimensional lossy wave equations to infer the spatial absorption coefficients and the wave velocities, which agree excellently with those derived from the dispersion relations.

Furthermore, the face-centered-cubic packings of equally-sized frictionless spheres are inserted into the fluid domain for simulating wave propagation in a saturated granular material. By activating/deactivating the hydrodynamics, it is proved that the presence of the pore fluid changes the dispersion relations from nonlinear to almost linear. The compressional- and shear-wave dispersion relations, which are uncoupled in dry face-centered-cubic configurations, become coupled under the influence of the hydrodynamic interactions with the solid particles. Among various input waveforms, the cosine leads to the cleanest signals in both the time- and frequency domains.

Finally, using the cosine for the acoustic source at the boundary, the compressional- and shear-wave dispersion relations are obtained under a wide range of effective confining pressures. The compressional- and shear-wave velocities qualitatively agree with the analytical solutions given by Biot's theory, with relative errors between 19.49% and 10.53% for the former and 3.52% to 0.15% for the latter, at effective pressure ranging from 0.1 MPa to 30 MPa. In addition to the fast compressional waves, the slow waves as predicted by Biot's theory are numerically reproduced in the LB-DEM simulations. Again, the cosine input waveform yields the cleanest signals which show clear correlations in time that indicate the existence of the slow waves.

In conclusion, the novel hydro-micromechanical model is a powerful tool that allows to explore physical coupling

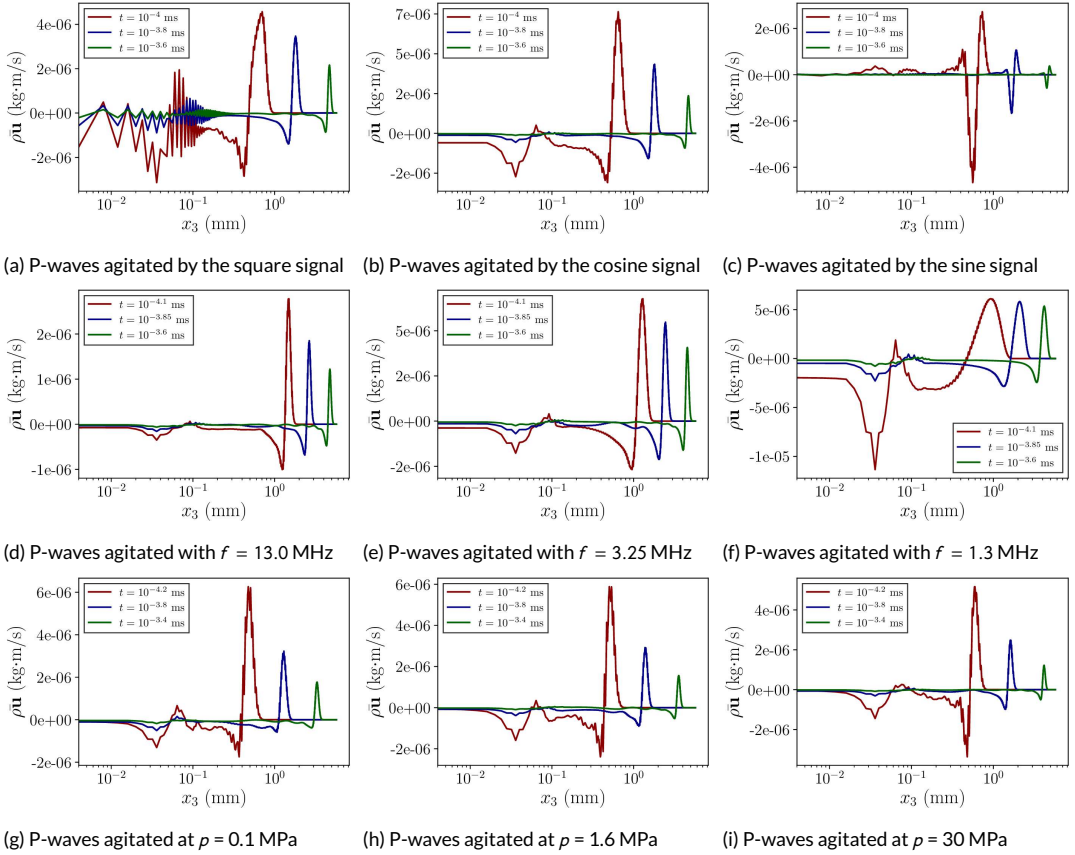


FIGURE 15 Fast and slow propagation of the average longitudinal momentum of the pore fluid along the x_3 direction at various time steps. The waveforms (a-c) and input frequencies (d-f) of the acoustic sources and the effective confining pressures on the FCC packings (g-i) are varied between the LB-DEM simulations.

mechanisms neglected by the conventional Biot's theory, and the influence of the input frequency from low to very high. As next step, detailed investigations of pore-scale squirt flow will be performed and the modified Biot's equations that take the squirt flow into account are needed. Moreover, the numerical tool allows to investigate the difference of wave velocities for initial random packing in dry and saturated configurations. Such comparison is very difficult to reproduce in experiments and often leads to disagreement with Biot's prediction based on the knowledge of the stiffness of the dry skeleton. Finally, it is straightforward to extend the algorithm to simulation a wide range of saturation degrees. Ongoing work on the methodological side aims at overcoming the lower limit of the relaxation time, which will make it possible to simulate wave propagation in fluids with realistic viscosities.

ACKNOWLEDGMENTS

We thank the Jülich Supercomputing Centre for the technical support and the allocated CPU time. We acknowledge support from the European Space Agency (ESA) contract 4000115113 'Soft Matter Dynamics' and the European Cooperation in Science and Technology (COST) Action MP1305 'Flowing matter'.

REFERENCES

- [1] Santamarina JC, Klein KA, Fam MA. *Soils and waves*. J. Wiley & Sons; 2001.
- [2] Clayton CRI. Stiffness at small strain: research and practice. *Géotechnique* 2011;61(1):5–37.
- [3] Alvarado G, Coop MR. On the Performance of Bender Elements in Triaxial Tests. *Géotechnique* 2011;62(1):1–17.
- [4] Zang A, Oye V, Jousset P, Deichmann N, Gritto R, McGarr A, et al. Analysis of induced seismicity in geothermal reservoirs - An overview. *Geothermics* 2014;52:6–21.
- [5] Altmann JB, Müller BIR, Müller TM, Heidbach O, Tingay MRP, Weißhardt A. Pore pressure stress coupling in 3D and consequences for reservoir stress states and fault reactivation. *Geothermics* 2014;52:195–205.
- [6] Gritto R, Jarpe SP. Temporal variations of Vp/Vs-ratio at The Geysers geothermal field, USA. *Geothermics* 2014;52:112–119.
- [7] Batzle M, Wang Z. Seismic properties of pore fluids. *Geophysics* 1992;57(11):1396–1408.
- [8] Kelder O, Smeulders DMJ. Observation of the Biot slow wave in water-saturated Nivelsteiner sandstone. *Geophysics* 1997;62(6):1794–1796.
- [9] Gu X, Yang J, Huang M, Gao G. Bender element tests in dry and saturated sand: Signal interpretation and result comparison. *Soils Found* 2015;55(5):951–962.
- [10] Camacho-Tauta JF, CASCANTE G, VIANA DA FONSECA A, SANTOS JA. Time and frequency domain evaluation of bender element systems. *Géotechnique* 2015;65(7):548–562.
- [11] O'Donovan J, O'Sullivan C, Marketos G, Muir Wood D. Analysis of bender element test interpretation using the discrete element method. *Granul Matter* 2015;17(2):197–216.
- [12] Lee JS, Santamarina JC. Bender Elements: Performance and Signal Interpretation. *J Geotech Geoenvironmental Eng* 2005;131(9):1063–1070.
- [13] Merkel A, Luding S. Enhanced micropolar model for wave propagation in ordered granular materials. *Int J Solids Struct* 2017;106:91–105.

- [14] Mouraille O, Mulder WA, Luding S. Sound wave acceleration in granular materials. *J Stat Mech Theory Exp* 2006;2006(07):P07023.
- [15] Marketos G, O'Sullivan C. A micromechanics-based analytical method for wave propagation through a granular material. *Soil Dyn Earthq Eng* 2013;45:25–34.
- [16] Cheng H, Shuku T, Thoeni K, Yamamoto H. Calibration of micromechanical parameters for DEM simulations by using the particle filter. *EPJ Web Conf* 2017;140:12011.
- [17] Cheng H, Shuku T, Thoeni K, Yamamoto H. Probabilistic calibration of discrete element simulations using the sequential quasi-Monte Carlo filter. *Granul Matter* 2018;20(1).
- [18] Cheng H, Shuku T, Thoeni K, Tempone P, Luding S, Magnanimo V. Iterative Bayesian filtering for fast and automated calibration of image-based DEM models. *Comput Methods Appl Mech Eng* 2018;(under review).
- [19] Güven I. Hydraulic and acoustical properties of porous sintered glass bead systems: experiments, theory and simulations. PhD thesis, University of Twente; 2016.
- [20] Strack OE, Cook BK. Three-dimensional immersed boundary conditions for moving solids in the lattice-Boltzmann method. *Int J Numer Methods Fluids* 2007;55(2):103–125.
- [21] Robinson M, Ramaioli M, Luding S. Fluid-particle flow simulations using two-way-coupled mesoscale SPH-DEM and validation. *Int J Multiph Flow* 2014;59:121–134.
- [22] Guo N, Zhao J. Parallel hierarchical multiscale modelling of hydro-mechanical problems for saturated granular soils. *Comput Methods Appl Mech Eng* 2016;305:37–61.
- [23] Jing L, Kwok CY, Leung YF, Sobral YD. Extended CFD-DEM for free-surface flow with multi-size granules. *Int J Numer Anal Methods Geomech* 2015;40(1):62–79.
- [24] Benzi R, Succi S, Vergassola M. The lattice Boltzmann equation: theory and applications. *Physics Reports* 1992;222(3):145–197.
- [25] T Krüger, Kusumaatmaja H, Kuzmin A, Shardt O, Silva G, Viggen EM. *The Lattice Boltzmann Method Principles and Practice*. Springer International Publishing, Cham, Zug, Switzerland; 2017.
- [26] Mansouri M, Youssoufi MSE, Nicot F. Numerical simulation of the quicksand phenomenon by a 3D coupled Discrete Element - Lattice Boltzmann hydromechanical model. *Int J Numer Anal Methods Geomech* 2017;41(3):338–358.
- [27] Zhang C, Soga K, Kumar K, Sun Q, Jin F. Numerical study of a sphere descending along an inclined slope in a liquid. *Granul Matter* 2017;p. 868–874.
- [28] Han Y, Cundall PA. Resolution sensitivity of momentum-exchange and immersed boundary methods for solid-fluid interaction in the lattice Boltzmann method. *Int J Numer Methods Fluids* 2011;67(3):314–327.
- [29] Rivas N, Frijters S, Pagonabarraga I, Harting J. Mesoscopic electrohydrodynamic simulations of binary colloidal suspensions. *J Chem Phys* 2018;148(14):144101.
- [30] Biot MA. General theory of three-dimensional consolidation. *J Appl Phys* 1941;12(2):155–164.
- [31] Biot MA. Generalized Theory of Acoustic Propagation in Porous Dissipative Media. *J Acoust Soc Am* 1962;34(9A):1254–1264.
- [32] Harting J, Frijters S, Ramaioli M, Robinson M, Wolf DE, Luding S. Recent advances in the simulation of particle-laden flows. *Eur Phys J Spec Top* 2014 Oct;223(11):2253–2267.

- [33] Noble DR, Torczynski JR. A Lattice-Boltzmann Method for Partially Saturated Computational Cells. *Int J Mod Phys C* 1998;09(08):1189–1201.
- [34] Rettinger C, Rde U. A comparative study of fluid-particle coupling methods for fully resolved lattice Boltzmann simulations. *Comput Fluids* 2017;154:74–89.
- [35] Yang GC, Jing L, Kwok CY, Sobral YD. A comprehensive study of coupled LBM-DEM with immersed moving boundary. *Int J Numer Anal Methods Geomech* 2018;(under review).
- [36] Hecht M, Harting J. Computational steering of cluster formation in Brownian suspensions. *Comput Math with Appl* 2009;58(5):995–1002.
- [37] Kunert C, Harting J, Vinogradova OI. Random-Roughness Hydrodynamic Boundary Conditions. *Phys Rev Lett* 2010 Jun;105:016001.
- [38] Cheng H, Yamamoto H, Thoeni K. Numerical study on stress states and fabric anisotropies in soilbags using the DEM. *Comput Geotech* 2016;76:170–183.
- [39] Cheng H, Yamamoto H, Thoeni K, Wu Y. An analytical solution for geotextile-wrapped soil based on insights from DEM analysis. *Geotext Geomembranes* 2017;45(4):361–376.
- [40] Erlend Magnus Viggen. The Lattice Boltzmann Method with Applications in Acoustics. PhD thesis, Norwegian University of Science and Technology; 2009.
- [41] Viggen EM. The lattice Boltzmann method : Fundamentals and acoustics. PhD thesis, Norwegian University of Science and Technology; 2014.
- [42] Zhuo C, Sagaut P. Acoustic multipole sources for the regularized lattice Boltzmann method: Comparison with multiple-relaxation-time models in the inviscid limit. *Phys Rev E* 2017;95(6):1–22.
- [43] Ladd AJC, Verberg R. Lattice-Boltzmann Simulations of Particle-Fluid Suspensions. *J Stat Phys* 2001;104(5/6):1191–1251.
- [44] Aidun CK, Lu Y, Ding EJ. Direct analysis of particulate suspensions with inertia using the discrete Boltzmann equation. *J Fluid Mech* 1998;373:S0022112098002493.
- [45] Zou Q, He X. On pressure and velocity boundary conditions for the lattice Boltzmann BGK model. *Phys Fluids* 1997;9(6):1591–1598.
- [46] Kutay ME, Aydilek AH, Masad E. Laboratory validation of lattice Boltzmann method for modeling pore-scale flow in granular materials. *Comput Geotech* 2006 dec;33(8):381–395.
- [47] Hecht M, Harting J. Implementation of on-site velocity boundary conditions for D3Q19 lattice Boltzmann simulations. *J Stat Mech Theory Exp* 2010;2010(01):P01018.
- [48] Mavko G, Mukerji T, Dvorkin J. The rock physics handbook, 1998. Cambridge Univ Press 1993;.
- [49] Ba J, Cao H, Du Q. Nonlinear Acoustic Waves in Fluid-Saturated Porous Rocks – Poro-Acoustoelasticity Theory. In: *Wave Process. Class. New Solids InTech*; 2012.
- [50] Otsubo M, O'Sullivan C, Hanley KJ, Sim WW. Influence of packing density and stress on the dynamic response of granular materials. *Granul Matter* 2017;19(3):50.
- [51] Cheng H, Luding S, Saitoh K, Magnanimo V. Elastic wave propagation in dry granular media: effects of probing methods and stress history. *Int J Solids Struct* 2018;(under review).
- [52] La Ragione L, Magnanimo V. Contact anisotropy and coordination number for a granular assembly: A comparison of distinct-element-method simulations and theory. *Phys Rev E - Stat Nonlinear, Soft Matter Phys* 2012;85(3).
- [53] Schmieschek S, Shamardin L, Frijters S, Krger T, Schiller UD, Harting J, et al. LB3D: A parallel implementation of the Lattice-Boltzmann method for simulation of interacting amphiphilic fluids. *Comput Phys Commun* 2017;217:149–161.